



Review

# Progress and Perspectives of Conducting Metal–Organic Frameworks for Electrochemical Energy Storage and Conversion

Minggui Li, Guangxun Zhang, Yuxin Shi, Huijie Zhou, Yongcai Zhang  and Huan Pang 

School of Chemistry and Chemical Engineering, Yangzhou University, Yangzhou 225002, China; lmingui2022@163.com (M.L.); gxzhangchem@163.com (G.Z.); syx13218968285@163.com (Y.S.); zhouhuijiezhj929@163.com (H.Z.); zhangyc@yzu.edu.cn (Y.Z.)

\* Correspondence: huanpangchem@hotmail.com or panghuan@yzu.edu.cn

**Abstract:** The metal–organic framework (MOF) is a kind of porous material with lattice materials. Due to its large surface area and structural diversity, it has made great progress in the fields of batteries, capacitors, electrocatalysis, etc. Conductive MOF (c-MOF) increases the conductivity based on the original advantages of the MOF, which is more suitable for the development of batteries, capacitors, electrocatalysis, and other fields. This review summarizes the preparation of c-MOF and the research progress of conductive MOFs in the field of electrochemical energy storage and conversion.

**Keywords:** conductive MOFs; supercapacitors; electrode materials; battery; electrocatalysis

## 1. Introduction

With sustainable energy development in the 21st century, electrochemical energy storage and conversion has become a new field competing for development at home and abroad. At the same time, electrochemical energy storage and conversion technology pave the way for sustainable energy development [1]. The more popular electric energy storage carriers are supercapacitors and various batteries. The electrode materials that can determine their energy density, conductivity, and capacitance have become the focus of research. Electrocatalysis is the key to the conversion of electric energy and chemical energy. Meanwhile, the consumption of non-renewable energy also promotes the development of sustainable energy conversion technology. Figure 1a shows the application of conductive MOFs in batteries, supercapacitors, and electrocatalysis, and also shows various metal ions combined with conductive MOF ligands. As shown in Figure 1b, the number of articles published by researchers in the field of conductive MOFs has increased year by year in the last ten years, and the conductive MOF has gradually become a hot research field. Figure 1c visually shows the percentage of conductive MOFs in various fields of energy storage and conversion.

In general, batteries and supercapacitors consist of electrodes, electrolytes, current collectors, and voltage dividers. The mechanism is that the charging or discharging process occurs under the action of the electrode materials by applying an appropriate potential between current collectors. The charge carrier connected to the circuit through the shunt is driven by potential energy. In the process of discharge, the electrostatic potential of the supercapacitor and the chemical energy of the battery are converted into electrical energy. In charging, electric energy is converted into potential and chemical energy. Supercapacitors have a high power density due to the rapid physical charging and discharging process between the electrode material and the electrolyte. What happens in batteries is a REDOX reaction, a slow chemical change, and batteries usually have a high energy density. The high power density and high energy density generally do not coexist [2]. Among them, the electrode is the key component that determines the performance of the supercapacitors



**Citation:** Li, M.; Zhang, G.; Shi, Y.; Zhou, H.; Zhang, Y.; Pang, H. Progress and Perspectives of Conducting Metal–Organic Frameworks for Electrochemical Energy Storage and Conversion. *Chemistry* **2023**, *5*, 2441–2475. <https://doi.org/10.3390/chemistry5040161>

Academic Editor: In Sun Cho

Received: 19 October 2023

Revised: 1 November 2023

Accepted: 3 November 2023

Published: 11 November 2023



**Copyright:** © 2023 by the authors. Licensee MDPI, Basel, Switzerland. This article is an open access article distributed under the terms and conditions of the Creative Commons Attribution (CC BY) license (<https://creativecommons.org/licenses/by/4.0/>).

and batteries. The electrode materials of supercapacitors and batteries usually involve key properties, such as electrical conductivity, porosity, surface area, chemical stability, and manufacturing cost. Therefore, choosing the appropriate electrode materials is the key strategy to make the electrochemical energy storage devices have better performance [3–9]. At the same time, the development of advanced electrochemical reaction electrocatalysts has an important meaning in the development of batteries, electrolysis, and electrocatalysis.



**Figure 1.** (a) Metal ions and electrochemical applications of conducting MOFs are reviewed. (b) The histogram of the number of articles published in the conductive MOF by year is incomplete. (c) Statistics on the percentage of conductive MOF materials in each area of study are incomplete.

Up to now, many carbon-based materials [10] (including activated carbon, carbon nanotubes, graphene, etc.), conductive polymers [11–13], MXenes [1], metal oxides [2], metal hydroxides [14], and metal sulfides [15] have been proved to be very promising electrode materials. However, each material has its advantages and limitations. For example, most carbon-based materials have good electrical conductivity and excellent structural/chemical stability. Although activated carbon has a large specific surface area, its amorphous structure is not suitable for adjusting the synthesis results. Conductive polymer has good specific capacitance, processability, and conductivity, but poor stability. MXenes have high conductivity and high specific volume capacitance, but their electrochemical window is relatively narrow; however, the large capacitance of metal oxides has the defects of poor cycle stability and relatively short life [16,17]. Due to the limitations of these materials, it becomes more and more important to find new and more perfect electrode materials.

Metal–organic frameworks (MOFs) have high crystallinity and good pore structures [18–21]. Due to its unique properties, the MOF has potential applications in the

field of electrochemical energy storage and conversion [22–28]. In addition, the shortcomings of MOF, such as low electrical conductivity, poor chemical stability, and relatively high manufacturing cost, limit its practical application in these fields [29]. Therefore, many modification strategies of MOF materials have been explored to improve their performance in conventional lithium batteries, supercapacitors, and electrocatalysis, especially to solve the main disadvantage of low conductivity [30–37].

The conductive metal–organic framework is a kind of crystal material formed by the self-assembly of metal ions and organic ligands. In addition to inheriting the advantages of large specific surface area, it possesses the controllable morphology and structure, regular pore structure, and rich active sites of common MOF materials. Conductive metal–organic frameworks also have high electrical conductivity and can be directly used as electrode materials without the need for other preparation processes. Conductive MOFs with monodisperse channels and controllable topology can be used as a new system for nanoscale computational simulation. Conductive MOF ligands include carboxylate, imidazole, azolate, sulfonate, etc. Common ones include: HITP = 2,3,6,7,10,11-hexamino-triphenyl, HAB = hexaminobenzene, HHTP = 2,3,6,7,10,11-hexahydroxytriphenyl.

At present, there are three strategies to improve the conductivity of MOF materials. The first is to develop different composites based on MOFs so that the properties of composites are better than those of individual components. The MOF composite partially solves the inherent problem of low electrical conductivity of the original MOF. However, this affects the excellent performance of MOFs in terms of surface area and porosity [38–40]. Secondly, the MOF derivatives obtained by in situ electrochemical conversion or pyrolysis generally have better performance than the original MOF. However, most MOF derivatives will lose their original adjustable chemical functional groups and good porosity. Finally, different types of organic ligands can be designed to generate new conductive MOFs. In addition to inheriting the advantages of ordinary MOF, conductive MOF also has high conductivity and can be used as an electrode material for electrocatalysis without other modifications. In particular, the highly ordered nanochannels in the conductive metal–organic framework can reduce the collision between ions and layers and improve the power density [17].

In this paper, the efforts to synthesize and design different conductive MOF materials in recent years, as well as the progress in the performance of batteries, supercapacitors, and electrocatalytic properties using conductive MOF electrodes are reviewed. We hope that this review will promote the development of new ideas for conducting MOFs in energy storage and transfer by absorbing knowledge and experience from reported studies [41].

## 2. Synthesis

So far, there are many methods to synthesize pure conductive MOFs. In this part, we mainly introduce the water bath method, interface method, solvothermal method, and other methods. Possible characterization methods are also briefly described [42].

### 2.1. Synthesis of Conductive MOFs

#### 2.1.1. Hydrothermal Method

The hydrothermal method refers to the method of preparing materials by dissolving and recrystallizing powder in a sealed pressure vessel with water as a solvent. Compared with other powder preparation methods, the powder prepared by the hydrothermal method has the advantages of complete grain development, small particle size, uniform distribution, light particle agglomeration, cheap raw materials, easy-to-obtain suitable stoichiometry, and crystal shape [43].

Hmadeh et al. made (CAT) by heating an appropriate amount of HHTP and the corresponding metal acetate by soaking in solution at 85 °C for 24 h [44]. The preparation method of CAT is to mix a certain proportion of HHTP (=2,3,6,7,10,11-Hexahydroxytriphenyl) with the corresponding metal (II) acetate hydrate in aqueous solution and heat it at 85 °C for 24 h to obtain needle-shaped crystals. CAT and Co(II) and Ni(II) ions form an extended

porous 2D skeleton, and the new crystalline material called metal catecholate (M-CAT) exhibits excellent chemical stability, thermal stability, and high porosity. Nam et al. prepared the positive electrode material of a water-based secondary battery according to the above synthesis method. The schematic diagram of the rechargeable Zn-2D MOF battery and the structure of  $\text{Cu}_3(\text{HHTP})_2$  are shown in Figure 2a.  $\text{Cu}_3(\text{HHTP})_2$  has a reversible capacity of  $228 \text{ mAh g}^{-1}$  at  $50 \text{ mAh g}^{-1}$  and maintains 75.0% of its initial capacity after 500 cycles at a high current density of  $4000 \text{ mAh g}^{-1}$  ( $\sim 18 \text{ C}$ ). The shape and macropore of the synthesized one-dimensional nanorod  $\text{Cu}_3(\text{HHTP})_2$  are beneficial to the diffusion of zinc ions (Figure 2b) [45]. Li and his team reported that a conductive MOF (Cu-CAT) was grown on carbon fiber paper to form nanowire arrays (NWA) in a controlled manner. The material can be directly used as an integrated electrode in supercapacitors and exhibits high porosity and excellent electrical conductivity [45]. Figure 2e shows the crystal structure of Cu-CAT. Copper ions coordinate with the HHTP ligand to form a 2D hexagonal lattice, which forms a cellular porous structure by model stacking. The effective orbital overlap makes Cu-CAT have good charge transport performance. Cu-CAT nanocrystals grown on carbon fiber paper uniformly cover the entire fiber (Figure 2f,g). According to the image, the nanowire is a hexagonal prism. As shown in Figure 2h, by comparing the performance of copper-based and carbon-based symmetric solid-state supercapacitors, this study shows that transforming the morphology of MOF materials into highly oriented nanowire arrays can significantly improve the electrochemical properties of MOF materials, such as the rate performance and capacitance, and make full use of their high porosity and good electrical conductivity.

Chen and his colleagues synthesized  $\text{Ni}_3(\text{HITP})_2$  through a simple water bath reaction, and it was modified by ultrasonic stirring in the dispersant [46]. The results show that  $\text{Ni}_3(\text{HITP})_2$  has a 2D layered crystal structure, hexagonal pore structure, and one-dimensional channel structure. However, it is not just tiny holes that help to improve material properties. The sodium-ion hybrid capacitors (SICs) studied by Dong et al. use a c-MOF,  $\text{Ni}_3(\text{hexaminobenzene})_2$  (Ni-MOF), as the electrode material [47]. Although Ni-MOF has a relatively large porous structure, it still needs sodium desolvation during discharge. On the shuttle effect in lithium–sulfur batteries, the 2D layered structure graphene-like  $\text{Ni}_3(\text{HITP})_2$  was synthesized by Cai et al. by  $\pi$ - $\pi$  conjugate. Its highly porous and effective physical barrier and chemisorption of polysulfide effectively inhibit the shuttle effect in the cycling process [48]. Figure 2i shows the synthesis of  $\text{Ni}_3(\text{HITP})_2$ , and it can be seen that it has a 2D lamellar structure. This structure not only provides high conductivity but also has uniform one-dimensional channels and abundant polar centers that can capture polysulfides.

Park and his team reported a new cobalt-based 2D conductive metal–organic framework, Co-HAB, for high-power energy storage devices, such as sodium-ion batteries. It can effectively solve the problems of low electron conductivity and poor stability under REDOX conditions [49]. Park et al. chose hexaminobenzene (HAB) as an organic linker to construct 2D conductive MOF (Figure 2m). Theoretically, HAB can carry out REDOX reactions with up to six electrons. This structure provides abundant and dense REDOX active centers. Figure 2n shows the three-position computational structure of Co-HAB and its three-electron reversible reaction. This work also proved for the first time that Co-HAB can store three electrons in organic electrolytes, thus showing relatively high specific capacity and relatively stable cycle life [50].

Generally, the hydrothermal method can only prepare oxide powder, but there is no in-depth research on the control of influencing the nucleation process and crystal growth process and satisfactory conclusions have not yet been obtained. The hydrothermal method needs high temperature and high pressure, which makes it highly dependent on production equipment, which also affects and hinders the development of the hydrothermal method. Therefore, the hydrothermal method tends to develop to low temperature and low pressure under hydrothermal conditions with temperature below  $100 \text{ }^\circ\text{C}$  and the pressure close to 1 standard atmospheric pressure.

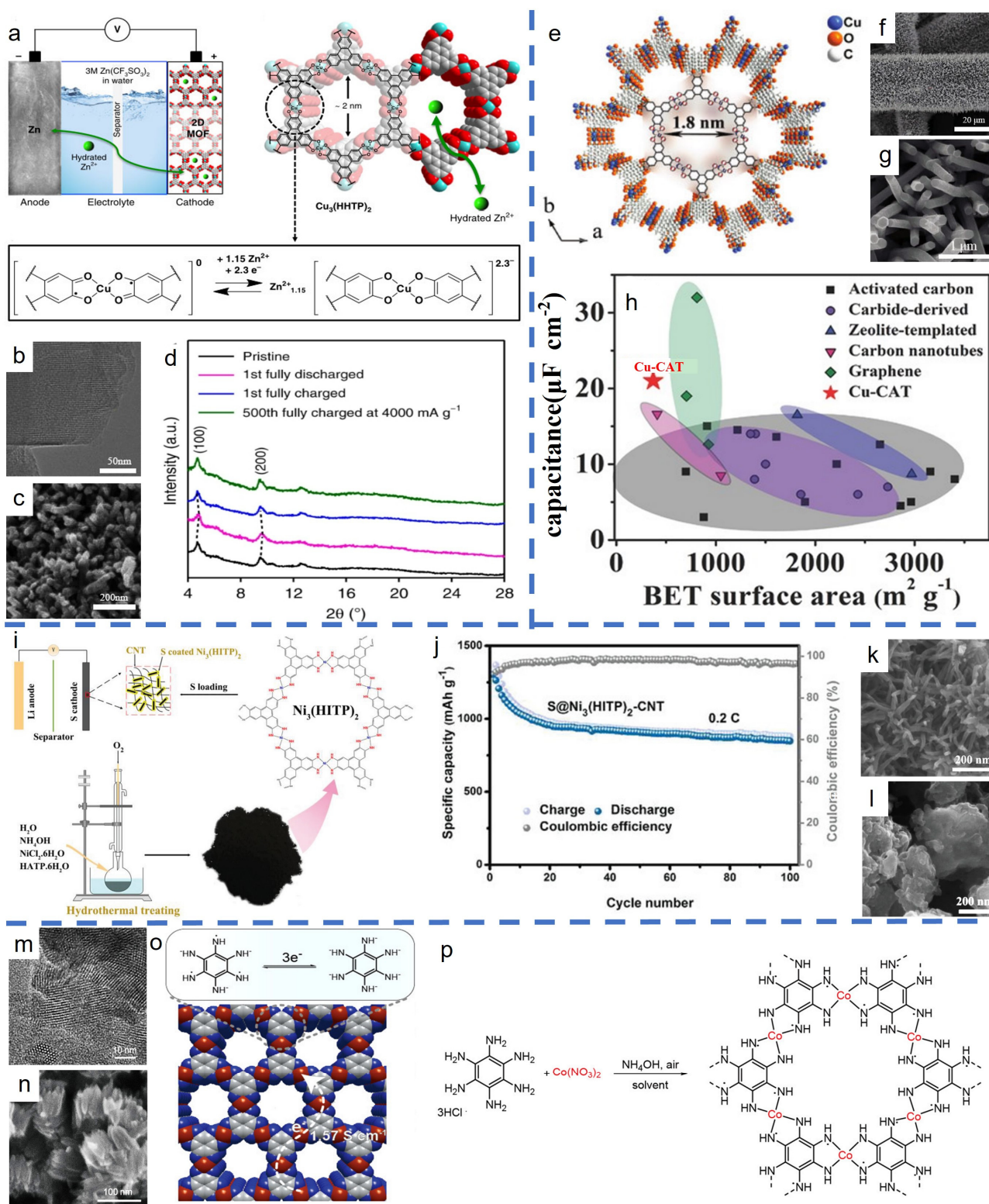


**Figure 2.** (a) Schematic illustration of the rechargeable Zn–2D MOF cell and structure of  $\text{Cu}_3(\text{HHTP})_2$ . (The cyan, red, and gray spheres represent Cu, O, and C atoms, respectively. The H atoms are omitted for the sake of clarity.) Expected redox process in the coordination unit of  $\text{Cu}_3(\text{HHTP})_2$ . (b) LD-HRTEM images at scale bars in 50 nm along the [010] direction. (c) Rietveld refinement of PXRD patterns. (d) PXRD patterns of the  $\text{Cu}_3(\text{HHTP})_2$  electrode in the pristine, first fully discharged/charged states at a rate of  $50\text{ mA g}^{-1}$ , and 500th fully charged states at a rate of  $4000\text{ mA g}^{-1}$ . (e) Crystal structure of Cu–CAT viewed along the *c*-axis. (f,g) SEM and photographic

image of the Cu–CAT NWAs growing on carbon fiber paper. (h) Performance comparison of Cu–CAT NWAs and carbon materials based on symmetric solid-state supercapacitors. (i) Schematic diagram of the synthesis of  $\text{Ni}_3(\text{HITP})_2$  and its application in Li–S batteries. (j) The cycling performance of  $\text{S@Ni}_3(\text{HITP})_2\text{-CNT}$  cathode at 0.2 C for 100 cycles. (k) The SEM images of  $\text{Ni}_3(\text{HITP})_2$  at 200 nm. (l) The SEM images of  $\text{S@Ni}_3(\text{HITP})_2$  at 200 nm. (m) Synthetic scheme of Co-HAB. (n) Three-electron reversible reaction in Co-HAB and the structure of Co-HAB in 3D. (o) HRTEM images of Co–HAB–D. (p) SEM images of Co–HAB–D. ((a–d) Reproduced with permission [46]. NATURE COMMUNICATIONS, 2019. (e–h) Reproduced with permission [48]. WILEY-VCH Verlag GmbH & Co. KGaA, Weinheim, 2017. (i–l) Reproduced with permission [51]. WILEY-VCH Verlag GmbH & Co. KGaA, Weinhei, 2019. (m–p) Reproduced with permission [52]. American Chemical Society, 2018.).

### 2.1.2. Solvothermal Method

The solvothermal method is the development of the hydrothermal method, which is different from the hydrothermal method in that the solvent used is an organic solvent instead of water. In the solvothermal reaction, by dissolving one or more precursors in a non-aqueous solvent, the reactants are dispersed in the solution and become more active under liquid or supercritical conditions. The reaction takes place and the product slowly forms. The process is relatively simple and easy to control, which can effectively prevent the volatilization of toxic substances and prepare air-sensitive precursors in a closed system [53].

Dincă and his team first used the solvothermal method to synthesize  $\text{Ni}_3(\text{HITP})_2$ . It is a pioneer in preparing  $\text{Ni}_3(\text{HITP})_2$  by the solvothermal method. The two-dimensional metal–organic skeleton  $\text{Ni}_3(\text{HITP})_2$  is synthesized by 2,3,6,7,10, 11-hexamine-triphenyl and  $\text{Ni}^{2+}$  in aqueous ammonia solution under aerobic conditions. The conductivity of the surface phase and bulk phase is 40 and  $2 \text{ S}\cdot\text{cm}^{-1}$ , respectively, which shows extraordinary conductivity by using two probes and van der Bau electrical measurement. As shown in Figure 3a, it is a synthetic diagram of  $\text{Ni}_3(\text{HITP})_2$ , and it is proved by elemental analysis and X-ray photoelectron spectroscopy that it is a diimine-pphenylquinone structure. Only the closed-shell resonance structures are shown, with the possible presence of a double radical nickelbisdiimide bond in  $\text{Ni}(\text{lsq})_2$  shown at the bottom. From the powder X-ray diffraction, it can be seen that  $\text{Ni}_3(\text{HITP})_2$  has an obvious crystal structure,  $2\theta = 4.7^\circ, 9.5^\circ, 12.6^\circ$ , and  $16.5^\circ$ , which proves that it is long-range ordered on the ab plane (Figure 3f). There is a weaker and wider peak at  $2\theta = 27.3^\circ$ , which proves that the long-range order in the direction is relatively poor. According to the information analysis in the figure, the possible stacking arrangement of two-dimensional pieces of  $\text{Ni}_3(\text{HITP})_2$  is AA or AB. The potential energy surface (PES) shown in Figure 3f is a Lagrangian polynomial obtained by interpolating the total DFT energy with 2D, which shows that the AA structure is asymmetric in energy, while the AB structure is the most stable. SEM analysis shows that the films grown on quartz substrate exhibit large pore surface characteristics and good coverage (Figure 3j,k). Finally, all these data prove that  $\text{Ni}_3(\text{HITP})_2$  is a hexagonal structure. The charge transport characteristics and potential excellent electrical properties of  $\text{Ni}_3(\text{HITP})_2$  deserve further study [51].

Shuai et al. designed a conductive MOF based on catechol, Ni–HHTP (HHTP = 2,3,6,7,10, 11–hexahydroxy triphenyl), which is beneficial to the synergistic enhancement of polysulfide chemisorption in Li–sulfur batteries, thus promoting the conversion of polysulfide in Li–sulfur batteries. The Ni–HHTP can not only inhibit the free diffusion of polysulfides but also reduce the adsorbed polysulfides to solid  $\text{Li}_2\text{S}$ . Thus, the utilization rate of active materials in lithium–sulfur batteries can be improved. The improvement of the performance of the Ni–HHTP@CP anode material battery is of great significance for the rational design of the lithium-ion battery anode material with the combination of strong polysulfide adsorption and good electronic conductivity. Figure 3b shows the synthesis of Ni–HHTP from  $\text{Ni}(\text{OAC})_2$  and 2,3,6,7,10,11–6 hydroxyphenyl (HHTP) under solvothermal conditions. Ni–HHTP is a bilayer structure. Level 1 punishes the male with the hexagonal top lacking snow, and level 2 unloads the top mountain. They form parallel one-dimensional channels

through p-p bond interactions and overlapping hydrogen bonds. Figure 3h shows the constant current–charging curves of the Ni–HHTP@Cp positive battery at 0.1, 0.2, 0.5, 1, and 2 °C [52].

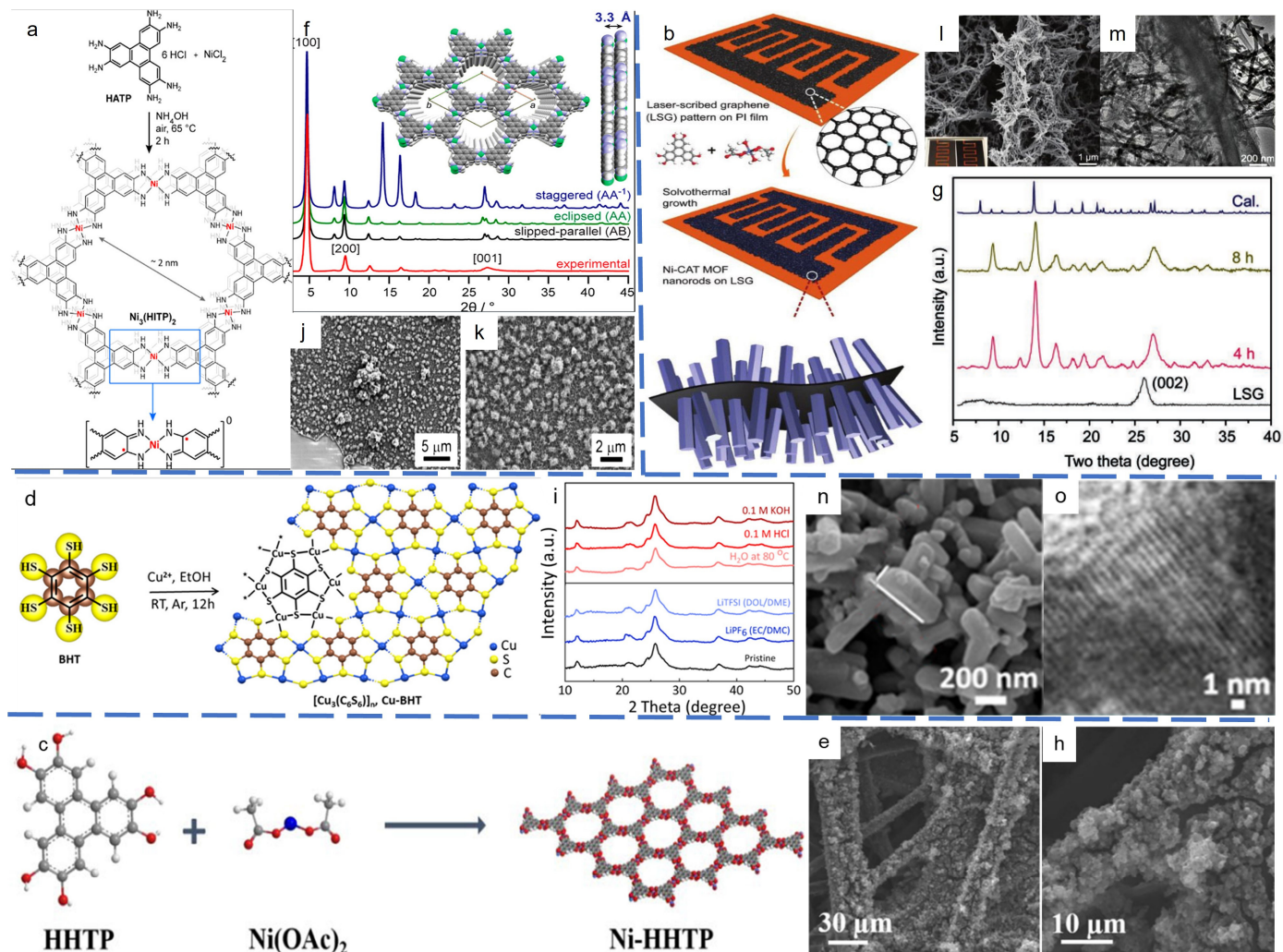


**Figure 3.** (a) Synthesis of  $\text{Ni}_3(\text{HITP})_2$ . (b) Schematic illustration of the LSG/Ni–CAT MOF hybrid. (c) Schematic illustration of the synthetic procedure of Ni–HHTP. (d) The synthesis process of the 2D Cu–BHT MOF. (e) A zoom–in representation of the Li–ion storage process at the Cu–BHT molecule. (f) Experimental and simulated PXR patterns of  $\text{Ni}_3(\text{HITP})_2$ . (g) XRD patterns of LSG and Ni–CAT MOF nanorods (baseline corrected). (h) Galvanostatic discharge–charge profiles of batteries with Ni–HHTP@CP cathode at 0.1, 0.2, 0.5, 1, and 2 C, respectively. (i) XRD patterns of the Cu–BHT powder after soaking in different solvents for 25 h. (j,k) SEM micrographs for films of  $\text{Ni}_3(\text{HITP})_2$  at various magnifications. (l) SEM images of LSG/Ni–CAT MOF. (m) TEM image of LSG/Ni–CAT MOF. (n) SEM image of Cu–BHT. (o) HRTEM image of Cu–BHT. ((a,f,j,k) Reproduced with permission [54]. American Chemical Society, 2014. (b,g,l,m) Reproduced with permission [55]. WILEY–VCH Verlag GmbH & Co. KGaA, Weinheim, 2019. (c,h) Reproduced with permission [56]. Science Press and Dalian Institute of Chemical Physics, Chinese Academy of Sciences, 2021. (d,e,i) Reproduced with permission [57]. American Chemical Society, 2020.).

Conductive 2D metal–organic frameworks (MOFs) have incomparable advantages in electrochemical applications. Hao and his team have developed a nickel-based MOF with good electrical conductivity, Ni–CAT, and they propose a new process for selectively growing Ni–CAT MOF on 3D laser-engraved graphene (LSG) [51]. They combined laser wounding with thermal growth in a low-temperature selective solvent to create a

symmetrical electrochemical micro-supercapacitor, which significantly improved its electrochemical behavior. Polyimide membrane, a carbon base, and 3DLSG was patterned directly to selectively grow Ni-CAT nanorods as a 3D conductive matrix. At the same time, the LSG/Ni-CAT-based supercapacitor shows good rate performance and cycle stability. The scanning electron microscope (SEM) image (Figure 3l) and TEM image (Figure 3m) show that the LSG films are porous, almost vertically intersected with polyimide substrates. The X-ray diffraction map reacted at 4 h and 8 h to record naked LSG and nano bar powder, and the results showed that increasing the holding time would lead to a decrease in crystallinity, which may reduce the electrochemical behavior of the electrode (Figure 3g). The work of Hao et al. showed that a conductive MOF can be used as an electrode for micro-supercapacitors in miniaturized energy storage systems.

Jie and his colleagues solved the limitation of aromatic heterocyclic conjugated molecules in lithium-ion batteries due to low conductivity and easy solubility in electrolytes by immobilization of the nitrogen-rich aromatic molecules tricyclic quinazoline (TQ) and CuO<sub>4</sub> units into a two-dimensional conductive metal-organic framework to release their ability to store lithium ions. The two-dimensional conductive MOF Cu-HHTQ was obtained by solvothermal synthesis of N, N-dimethylformamide (DMF) and water at 858 °C for 24 h. It facilitates Li<sup>+</sup>/e<sup>-</sup> transport and ensures that the electrode is elastic, resulting in a high capacity of 657.6 mAhg<sup>-1</sup> at 600 mAhg<sup>-1</sup>, with good magnification capacity and excellent circularity [58]. In Jamie's research, by studying the capacitive properties of Cu<sub>3</sub>(HHTP)<sub>2</sub> and acetonitrile-based electrolytes, some basic problems of applying two-dimensional conductive MOF to electric double-layer capacitors are expected to be solved. These include: the influence of capacity performance by metal defects or the properties of organic bonding molecules on capacity performance is limited in draw-type MOF. They found that at a current density of 0.04–0.05 Ag<sup>-1</sup>, the capacity was increased twice as much as that of 110–114 Fg<sup>-1</sup>. Meanwhile, by comparing Cu<sub>3</sub>(HHTP)<sub>2</sub> with the previously reported analog Ni<sub>3</sub>(HITP)<sub>2</sub>, the results show that organic binding molecules with almost the same properties or structures as metal nodules are largely unrelated to the permittivity of MOF. A limited stable bilayer voltage window of 1 V was found, with 30,000 cycles, and the median capacity retention rate was 81% [59]. Using divalent copper salt and benzenhexaethylol salt (BHT) as precursors, Zhenzhen et al. synthesized a two-dimensional conductive metal-organic skeleton with REDOX properties, Cu-BHT, which has a theoretical capacity of 236 mAhg<sup>-1</sup> in lithium-ion batteries. The Cu-BHT anode has an excellent reversible capacity of 175 mAhg<sup>-1</sup> at a high current density of 300 mAhg<sup>-1</sup> and an ultra-low capacity degradation (0.048%/time) after 500 cycles. The Cu-BHT MOF is synthesized in the Figure 3d format. Without adding any additives, the BHT monomer reacts with the divalent copper ion salt in an ethanol solution, and the final powder obtained is nearly three times higher than that obtained by the interfacial method. As shown in Figure 3e, this represents the lithium-ion storage process on the Cu-BHT molecule. As an excellent cathode material, excellent lithium storage performance can be obtained even in a short charge-discharge time. The thermogravimetric analysis curves show that Cu-BHT has good thermal stability up to 456 °C. The PXRD spectrum shows that the crystallinity of Cu-BHT remains good under different electrolyte conditions (Figure 3i). Compared with conventional MOF, Cu-BHT can withstand a wider PH range, rapidly changing REDOX conditions in the battery, and the complex electrolyte composition. Based on the excellent REDOX properties and cycle stability of the Cu-BHT electrode, they concluded the possible reasons: the ideal diffusion path of lithium ions and electrons in the lattice; intrinsic electronic conductivity; BHT interacts with Cu through the coordination of d-π conjugate. If a semi-battery cathode with Cu-BHT was used, the high theoretical capacity of 236 mAhg<sup>-1</sup> was obtained based on the four-electron reactions from 3.0 V to 1.5 V (VS Li<sup>+</sup>/Li). When the current density was 50 mAhg<sup>-1</sup>, the specific capacity was 232 mAhg<sup>-1</sup>, and the REDOX active centers on Cu-BHT were fully utilized. With current densities of 300 mA g<sup>-1</sup> and 1000 mA g<sup>-1</sup>, Cu-BHT demonstrated ultra-long cycle stability and magnification capacity of 500 cycles, which is superior to bulk organic polymer and



MOF anode materials. During the second Li-ion exchange at  $300 \text{ mAhg}^{-1}$ , this cathode had a discharge/charge capacity of  $175 \text{ mAhg}^{-1}$  with a Coulomb efficiency of approximately 100%, which corresponds to 75% of the theoretical capacity. At the same current density, it can maintain 94% capacity in the first 100 cycles. Research by Zhenzhen et al. showed that Cu-BHT is a promising cathode material for the next-generation lithium-ion battery [60].

At present, the solvothermal synthesis challenge has the advantages of large scale, high efficiency, and low cost, but it also has some limitations [61]. These limitations include: the solvothermal method is particularly sensitive to solvent, temperature, and reaction time, and harsh on experimental conditions; the generated crystals are usually polycrystalline powders or tiny single crystals, which makes them unable to be integrated into efficient electronic devices. Some reactions require high temperatures and long periods (days), resulting in huge energy costs [62].

### 2.1.3. Interfacial Method

The interface method is a synthetic method that reacts at the interface of two phases. It is generally used to prepare nanowire arrays or multilayers with uniform surfaces and controllable thickness (from microns to centimeters) [54,63].

$\text{Ni}_3(\text{HITP})_2$  is a conductive MOF with relatively good conductivity and stability so far.  $\text{Ni}_3(\text{HITP})_2$  films prepared by the interfacial method show excellent performance in supercapacitors and batteries. Weiwei et al. prepared  $\text{Ni}_3(\text{HITP})_2$  films by the gas-liquid interface method and used them as capacitive electrodes for flexible transparent supercapacitors. The  $\text{Ni}_3(\text{HITP})_2$  electrode has excellent photoelectric and optical properties including a Watermark rate (T) of 78.4%, ionic resistance ( $r_s$ ) of  $51.3 \text{ OHMsq}^{-1}$ , and surface weight (CA). The drawing speed of  $1.63 \text{ mFcm}^2$ , is  $5000 \text{ V}^{-1}$ . Compared with most known flexible supercapacitors, flexible transparent symmetric or asymmetric supercapacitors with  $\text{Ni}_3(\text{HITP})_2$  as electrodes can show higher surface capacitance and multiplication performance. As shown in Figure 4a, the structure design and general synthesis method of the  $\text{Ni}_3(\text{HITP})_2$  electrode were synthesized by the gas-liquid interface method.  $\text{HITP} \cdot 6\text{HCl}$  and  $\text{NiCl}_2 \cdot 6\text{H}_2\text{O}$  solution were mixed and heated to  $60 \text{ }^\circ\text{C}$ , and then  $\text{NH}_3 \cdot \text{H}_2\text{O}$  was added to the plane of the mixed solution. A  $\text{Ni}_3(\text{HITP})_2$  film is formed uniformly at the gas-liquid interface, and ITO/PET is covered on the surface (Figure 4b). The electrochemical properties of the electrodes with different reaction times were tested in a three-electrode system. From the cyclic voltammetry curve with a scanning rate of  $10 \text{ mVs}^{-1}$ , it can be seen that the current density increases with the increase in active material loading from 3 min to 60 min (Figure 4d). The GCD curve in the figure also shows the same trend. The reason for this phenomenon is that the capacitance activity becomes better with the increase in the active materials, but there is a limit. After 50 min, the film will have serious cracks, which will hinder the effective electron transmission, thus weakening the capacitive activity. The electrochemical capacitance of the  $\text{Ni}_3(\text{HITP})_2$  electrode prepared at 30 min was comprehensively evaluated. The corresponding GCD curves have a triangular profile when the current density is increased by 40 times ( $200 \text{ L cm}^2$ ), and the surface capacitance ( $1.0 \text{ LF cm}^2$ ) remains at 61.3%, indicating good reversibility, ideal capacitance behavior, and high-rate capacity in the charging and discharging process [55,57,64–66]. The study of Weiwei et al. provides a new idea for exploring the application of conductive MOF  $\text{Ni}_3(\text{HITP})_2$  films as electrode materials in flexible transparent supercapacitors [57]. In the production of  $\text{Ni}_3(\text{HITP})_2$  electrode materials by the gas-liquid method, there are also Guo et al.'s applications in the research of FET. Scanning electron microscopy (SEM) and atomic force microscopy (AFM) showed that the top surface of their films was flat, dense, and uniform, with an RMS roughness of about 1 nm [54].

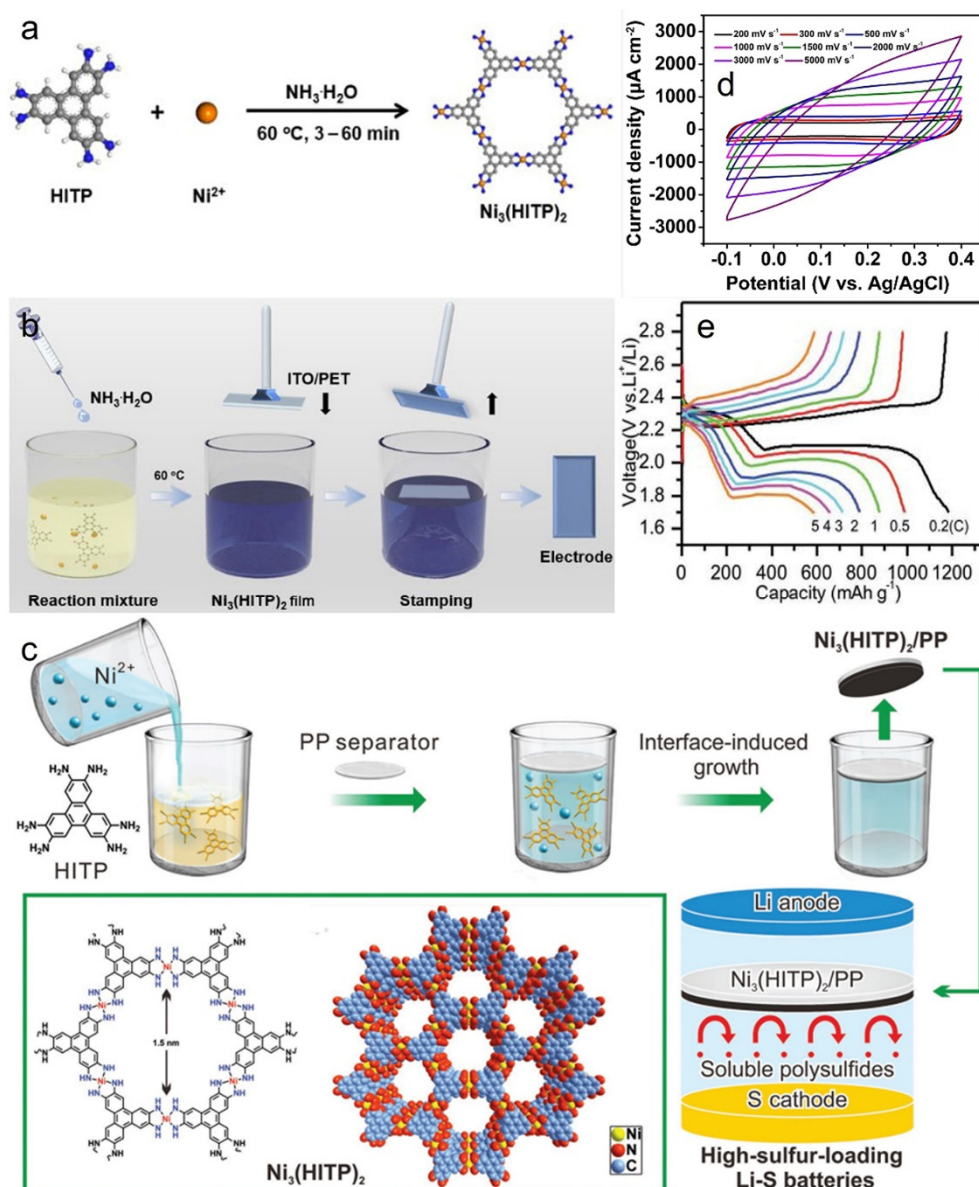


**Figure 4.** (a) General synthesis route of  $\text{Ni}_3(\text{HITP})_2$  MOF. (b) Schematic diagram of the  $\text{Ni}_3(\text{HITP})_2/\text{ITO}/\text{PET}$  electrode prepared by the Langmuir–Schaefer method at the gas–liquid interface. (c) Schematic representation of  $\text{Ni}_3(\text{HITP})_2$ -modified separator growth at the liquid–solid interface on a lithium–sulfur battery. (d) CV curves of  $\text{Ni}_3(\text{HITP})_2$  electrodes at scan rates of 200, 300, 500, 1000, 1500, 2000, 3000, and 5000 mV/s, respectively. (e) Charge and discharge curves of  $\text{Ni}_3(\text{HITP})_2/\text{PP}$  at rates of 0.2, 0.5, 1, 2, 3, 4, and 5 C, respectively. ((a,b,d) Reproduced with permission [67]. Science China Press. Published by Elsevier B.V. and Science China Press, 2020. (c,e) Reproduced with permission [68]. WILEY-VCH Verlag GmbH & Co. KGaA, Weinheim, 2018).

Ying and his team used the liquid–solid interface method to fabricate crystalline microporous membranes. When the  $\text{Ni}_3(\text{HITP})_2$  film is grown on an industrial diaphragm in situ, the MOF film has good affinity, larger than surface area, and is more conductive, which can significantly improve the capacity, cycle stability, and rate performance of lithium–sulfur batteries. Their  $\text{Ni}_3(\text{HITP})_2$  film, which was directly prepared on a commercial separator, significantly improved the ratio and cycle performance. Figure 4c shows the growth process of a  $\text{Ni}_3(\text{HITP})_2$ -modified diaphragm induced by the interface on a lithium–sulfur battery. It can be seen that  $\text{Ni}_3(\text{HITP})_2$  has a 2D layered structure and uniform one-dimensional channels.  $\text{Ni}_3(\text{HITP})_2$  grown directly on commercial polypropylene (PP) substrates can be

used directly in lithium–sulfur batteries. According to the SEM, primitive (PP) thin films have a very porous structure with angular diameters ranging from tens to hundreds of nanometers. The surface is covered with two layers of relatively dense  $\text{Ni}_3(\text{HITP})_2$ , and there is a small hole on the right. To evaluate the polysulfide adsorption performance of  $\text{Ni}_3(\text{HITP})_2$ , compared with conventional materials (such as graphene, carbon nanotubes (CNT), carbon black (CB), MOF HKUST-1, and ZIF-8),  $\text{Ni}_3(\text{HITP})_2$  has a much stronger ability to capture polysulfide than the other five materials, as shown in Figure 4e. The liquid–solid interface method proposed by Ying et al. provides a new idea for preparing large areas, relatively controllable thickness, and crack-free MOF films [65]. Shengyang and his colleagues used the liquid–solid interface method to grow Ni-MOF on cellulose nanofibers (CNF) and obtained CNF@Ni-MOF hybrid nanofibers, which showed high electrical conductivity and graded microporous structure up to  $100 \text{ S}\cdot\text{cm}^{-1}$ . The supercapacitor assembled with hybrid nanofibers as electrodes has high cycle stability, and the capacity retention rate is as high as 99% after continuous charging and discharging 10,000 times [69]. Tetsuya et al. synthesized Ni-BHT through the coordination reaction between benzenhexaethiol (BHT) and nickel acetate [ $\text{Ni}(\text{OAc})_2$ ]. The gas–liquid and liquid–liquid interface reactions are used to realize the controllable coordination between the two components [70].

Victor and his team used a liquid–liquid interface method to fabricate an ultrathin MOF film, Cu-CAT, with a thickness of 10 nm. They use self-assembled monolayer substrate modification and bottom-up technology to fabricate ultrathin MOF films with preferred orientation and use them as semiconductor materials [56]. Xing et al. used the solid–solid interface method to grow a conductive MOF  $\text{Cu}_3(\text{HHTP})_2$  nanowires array in situ at the interface between solid copper foil and a solid organic precursor, to some extent overcoming the difficulties of the high biochemical temperature of organic ligands and low decomposition temperature of conductive MOF. Using the  $\text{Cu}_3(\text{HHTP})_2$  nanowire array as a symmetrical electrode, the normalized capacitance of surface area is higher than that of most previous carbon materials. Their research extends the previous liquid or gas reaction to solid–solid reactions, providing a broader scope for the preparation and application of conductive MOF and its supercapacitors [71].

Compared with the c-MOF films prepared by the solvothermal method, the MOF films prepared by the interfacial method are smoother and denser, and the nanowire arrays prepared by the interfacial method have orderly structure and high crystallinity. However, conductive MOF prepared by each method has its disadvantages: the liquid–liquid interface method is not easy to adjust the film thickness and direction; the roughness of films prepared by the gas–liquid interface method is usually random; the solid–liquid interface method requires a high substrate before deposition; the solid–solid interface method is only suitable for gaseous organic linkers. In short, the interface method is not suitable for mass production [17].

#### 2.1.4. Other Methods

In addition to the widely used methods described above, unique methods to improve the conductivity of MOFs are being developed. Pingping et al. reported the preparation of a conductive MOF, Cu-CAT-1, by the oxygen-assisted cathodic method, whose uniform film was synthesized at the cathode. The electroplating of copper is avoided by oxygen reduction. The thickness of the films is usually between 70–1700 nm [72]. Since the products prepared by the solvothermal method were not completely uniform, smooth, and dense, Choi and Park proposed a method for defect repair, which used the same linker to repair the defects and then prepared  $\text{Cu}_3(\text{HAB})_2$  with high crystallinity. The conductivity was  $1.56 \times 10^{-2} \text{ S}\cdot\text{cm}^{-1}$ , which is nearly 700 times higher than that without treatment [73]. The defect repair method is a post-processing method, which is used to make up for the defects prepared by traditional methods, to improve the performance of conductive MOFs. However, this method is only effective when it is used to repair defects caused by inadequate synthesis [74]. Leily and her colleagues prepared a conductive MOF, Cu-THQ, by liquid phase stripping and applied it to a cathode material for Li–oxygen batteries, which

showed better performance in terms of sustained low charging potential than reported non-conductive MOF-based and MOF-derivative positive batteries. Cu-THQ was applied to the Li-O<sub>2</sub> battery system, using Cu-THQ NFS, 1 M LiNO<sub>3</sub>, 0.1 M InBr<sub>3</sub>, and TEGDME solvents. The HRTEM image clearly shows the dense and uniform pore structure arranged in a honeycomb pattern, with an average of less than 1 nm (Figure 5d). Figure 5g shows the charge-discharge curve of a battery with a capacity of 2000 mAhg<sup>-1</sup> and a current density of 1 A g<sup>-1</sup>. When the discharge point reaches the cut-off voltage of 2.5 V, that is, after 150 cycles, the battery cycle stops. Figure 5h shows the results obtained with a limited capacity of 2000 mAh g<sup>-1</sup> and a current density of 2 A g<sup>-1</sup>. The battery can discharge 100 cycles [75]. Similarly, Rashid and his team obtained a multilayer conductive MOF by stripping n-butyl lithium from an n-hexane solution in a liquid phase, which is a conventional hydrothermal synthesis method based on Co<sub>3</sub>(HITP)<sub>2</sub>. The specific surface area increased from 856 to 2338 m<sup>2</sup> g<sup>-1</sup>, and the electrical conductivity reached 67.8 S·cm<sup>-1</sup>. The product had excellent electrochemical performance and good cycle stability, and the capacity retention rate can reach 85% after 10,000 cycles [76]. The liquid stripping method is also a post-treatment method, which can improve the specific surface area and electrical conductivity without changing the structure of the conductive MOF. However, this method is usually only suitable for 2D nanosheets, and the solvent used for stripping is not common and may be dangerous.

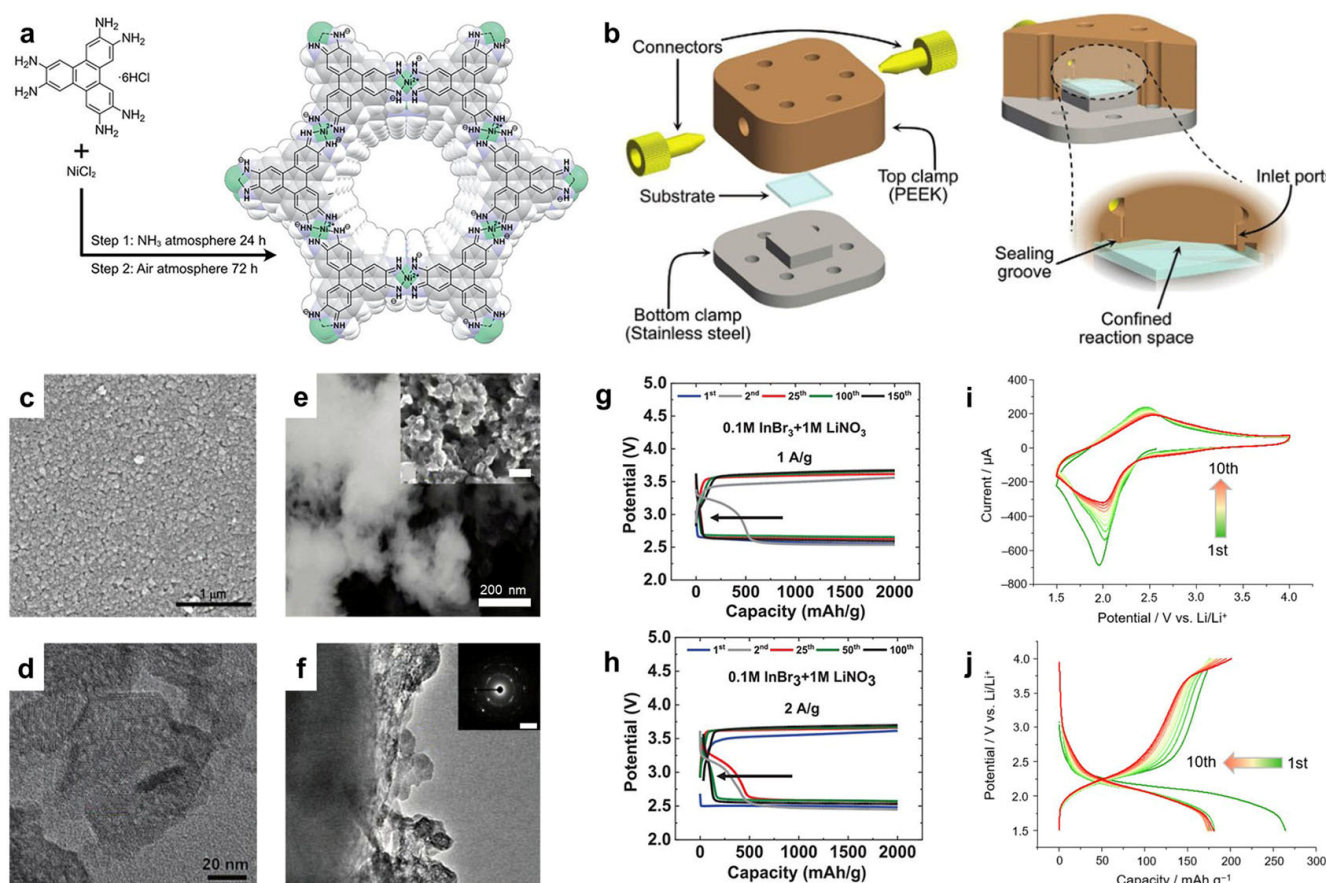


**Figure 5.** (a) Diagram of the synthesis path of Ni<sub>3</sub>(HITP)<sub>2</sub>. (b) Expansion of the microfluidic device. (c) SEM image of Ni<sub>3</sub>(HITP)<sub>2</sub> film grown on a quartz substrate. (d) Transmission electron microscope image of Cu-THQ MOF. (e) Scanning electron microscopy (SEM) image of the cathode after the tenth discharge of Cu-THQ as the positive electrode of the Li-O<sub>2</sub> battery running at 2 A g<sup>-1</sup> in a solvent containing 1 M LiNO<sub>3</sub>, 0.1 M InBr<sub>3</sub>, and TEGDME. Inset is a SEM image of the cathode after the tenth charge. (f) Transmission electron microscope image of the cathode after the tenth discharge of Cu-THQ as the positive electrode of the Li-O<sub>2</sub> battery running at 2 A g<sup>-1</sup> in a solvent containing

1 M LiNO<sub>3</sub>, 0.1 M InBr<sub>3</sub>, and TEGDME. The inset is a diffraction pattern of a Cu-THQ catalyst. (g) Charge and discharge voltage distribution of Cu-THQ in Cu-THQ NFS, 1 M LiNO<sub>3</sub>, 0.1 M InBr<sub>3</sub>, and TEGDME solvents in a battery with a current density of 1 Ag<sup>-1</sup>. (h) Charge and discharge voltage distribution of Cu-THQ in a 2 Ag<sup>-1</sup> current density cell. (i) Solid-state cyclic voltammetry image of cathode material at scanning speed of 0.5 mV s<sup>-1</sup>. (j) Charge-discharge characteristics of Fe(dhbq) at 0.1 C, or 28 mA g<sup>-1</sup>. ((a-c) Reproduced with permission [71]. Wiley-VCH GmbH, 2021. (d,g,h) Reproduced with permission [77]. Wiley-VCH GmbH, 2021. (i,j) Reproduced with permission [78]. American Chemical Society, 2021.).

Noemi et al. demonstrated that microgravity effects in a space station can be simulated on the ground using a microfluidic device. This microfluidic method is also used to prepare 2D c-MOF Ni<sub>3</sub>(HITP)<sub>2</sub> films. Figure 5a is a schematic diagram of the synthesis path of Ni<sub>3</sub>(HITP)<sub>2</sub>. The reaction took place in the device shown in Figure 5b. Under these conditions, the formed Ni<sub>3</sub>(HITP)<sub>2</sub> has almost no defects, and the film shows conductivity up to 40 S cm<sup>-1</sup> in a wide range. Scanning electron microscopy showed that the films were smooth, dense, and continuous without cracks, with a uniform thickness of about 100 nm (Figure 5c). This method of simulating a microgravity environment can control the thickness and orientation of a 2D molecular skeleton to a certain extent. However, at present, this method is not popular, and there are certain requirements for the experimental equipment [67]. Kon and his colleagues reported a rare electron conduction MOF, Fe(DHBQ), which was oxidized by in situ air. The electrochemical behavior of the compounds was studied by solid-state voltammetry. The reduction peak observed at 2.1 V corresponds to the two-electron reduction of the (DHBQ) ligand. The oxidation peak observed at 2.4 V may be related to the two-electron reduction process (Figure 5i). The constant-current characteristics are studied by using a half-cell configuration. As shown in Figure 5j, Fe(DHBQ) is relatively stable in the 2.0–2.2 V range, which corresponds to the two-electron reduction process of the (DHBQ) ligand [68]. Lu and his team used an anodic electrodeposition method to fabricate homogeneous 2D c-MOF, NiPc-MOF, on nickel foam and directly applied it to the electrodes of supercapacitors without adding any additives. The synthesized NiPc-MOF has a high conductivity of about 0.2 S cm<sup>-1</sup> and a large specific surface area of about 593 m<sup>2</sup> g<sup>-1</sup>, which makes it a promising electrode material for supercapacitors. This electrochemical deposition technology allows 2D c-MOF to grow in situ on the substrate without the need for binders and conductive additives. Its reaction conditions are mild and all parameters can be precisely controlled, but this method has not been widely used [79]. These methods are effective in preparing c-MOF, but they cannot be widely used due to their defects. Many methods still need to be studied and exploited. The characteristics and synthesis methods of common conductive MOFs are shown in Table 1.

**Table 1.** Characteristic and synthesis methods of conductive MOFs.

Material	Method	$\sigma$ [S·cm <sup>-1</sup> ] (300 K)	SSA[m <sup>2</sup> g <sup>-1</sup> ]	Ref.
Cu-BHT	Interface synthesis method	1414		[80]
Cu-BHT	Interface synthesis method	1005–1532		[81]
Ni-HAB	Solvothermal method	0.7	≈180–350	[82]
Cu-HAB	Solvothermal method	0.11	≈180–350	[82]
Zn-HAB	Solvothermal method	$8.6 \times 10^{-4}$	≈145	[83]
Cu-HHTP	Interface synthesis method	$1 \times 10^{-4}$	334	[56]
Ni <sub>3</sub> (HITP) <sub>2</sub>	Solvothermal method	58.8	766	[84]
Cu <sub>3</sub> (HHTP) <sub>2</sub>	Liquid-phase epitaxial method	0.02		[85]
Co <sub>3</sub> (HITP) <sub>2</sub>	Solvothermal method	11.5	281	[85]
Cu <sub>3</sub> (HHTQ) <sub>2</sub>	Solvothermal method	0.005	516.99	[86]
NiPc-Ni	Solvothermal method	$7.22 \times 10^{-4}$	101	[77]
NiPc-Cu	Solvothermal method	$1.43 \times 10^{-2}$	284	[77]

## 2.2. Characterization of *c*-MOFs

Since the first conductive MOF was synthesized in 2014, the research on conductive MOFs has made some progress. At the same time as synthesizing materials, the characterization of materials is also important [17]. The measurement of the conductivity, specific surface area, pore size distribution, crystal morphology, and size of the conductive MOF also has a key impact on the material properties and the continued development and application of the materials in the future [87]. Among them, the electrical measurement has a certain challenge, as electrical performance not only depends on the material itself, but also on the electrical wire, contact solder paste, substrate, and other material manufacturing devices which may have a significant impact on it [78,88].

Some basic characterization techniques and schemes include: (1) single-crystal X-ray diffraction (XRD), which can give relatively accurate structural information; (2) powder X-ray diffraction which can determine the phase purity and crystallinity of materials; (3) the adsorption/desorption isotherm of nitrogen determines the spacing and calculates the surface area; (4) SEM can measure the size and morphology of crystals and, combined with energy-dispersive X-ray spectroscopy, measure the composition and distribution of elements; (5) inductively coupled plasma optical emission spectroscopy is used to determine the purity and elemental ratio of the sample; (6) NMR spectroscopy can quantify the ratio of the mixed junctions in the MOF to determine the overall purity of the sample [87].

**Powder X-ray diffraction:** allows for the determination of MOF crystallinity. After the crystallinity is determined, the size of the unit cell can be determined. The phase purity of MOF can be determined by comparing this pattern with the single-crystal X-ray diffraction pattern [89]. The powder sample is placed on a sample rack made of plastic, glass, or aluminum. The method is used to prepare PXRD analysis samples.

**Single-crystal X-ray diffraction:** a method used to determine the structure of MOF. However, only when the crystal size is larger than 5–10  $\mu\text{m}$  can reliable data be collected. Single-crystal X-ray diffraction should be used only in coordination with other characterization methods.

**Nitrogen adsorption and desorption isotherms:** the MOF needs to be activated to collect isotherms. According to experience, only when the sample size multiplied by the specific surface area of the sample is greater than or equal to 100 square meters can reliable data be obtained, but sometimes it is not absolute [90,91].

**Scanning electron microscopy:** most MOF materials have poor electrical conductivity, which will affect the quality of SEM images undercharging. The most common method is to coat the sample with a conductive material. Higher resolution images can be obtained under the electron beam acceleration voltage, but surface defects or pollution details cannot be seen. Excessive acceleration voltage will increase the local temperature rise and may damage the crystal structure of the MOF.

**Analysis of the luminescence spectrum by inductively coupled plasma:** although ICP-MS can be used to detect very low concentrations, it is best to process a relatively large number of samples in a higher concentration range.

**NMR spectroscopy:** most MOFs are insoluble in conventional NMR solvents. Similar to inductively coupled plasma emission spectroscopy (ICP-AES) analysis, the sample must be completely dissolved to be meaningful. Solid nuclear magnetic resonance spectroscopy can also characterize MOFs, especially in detecting the local chemical environment within MOFs [92–94]. This method can be used to characterize specific functional groups or chemical states in MOFs [95].

**Thermogravimetric analysis:** since the decomposition path of the MOF may be different in different environments, it is very important to choose the measured gas atmosphere when measuring the thermal stability of the MOF. Similarly, thermogravimetric measurement needs to be combined with other characterization methods, including PXRD and adsorption measurement of materials at different temperatures to ensure the stability of MOF materials at different temperatures [96,97].

Aqueous stability testing: the functional groups of most MOFs are not necessarily neutral, but most likely alkaline or acidic, so a certain amount of water should be added before each test. The pH value of the water was tested before adding the MOF and after MOF filtration to ensure the accuracy of the results. Solutions for measuring pH values should also be configured with sodium hydroxide or hydrogen chloride, respectively, and the misleading effect of buffer and counter ions on the experimental results should be taken into account [98,99].

As mentioned earlier, the measurement of electrical conductivity is not mature because it depends on the equipment conditions. The definition states that conductivity requires the measurement of the conductance (G), length (L), and area (A) of the conducting channel:

$$\sigma = G L/A = I/V \times L/A, \quad (1)$$

Since conductance follows Ohm's law, measuring conductance requires either a ratio between current (I) and voltage (V) or a linear I–V curve. However, it should be noted that to make the I–V curve linear, you must keep the current or voltage as small as possible, because this is the only way that Ohm's law works [100]. Dincă et al. describes the measurement techniques for electrical conductivity, which they divided into the two-contact method, four-contact method, four-point method, and van der Wave method [101,102]. Since the two-contact method measures the total resistance of the material, wire, and shock, the resistance of the material to be measured must be much greater than that of the measuring equipment and contacts to avoid errors. The four-contact method and the van der Wave method can eliminate the electric shock and wire resistance, so they can be better applied to the conductive MOF with high conductivity [101]. The shape of the MOF has a great influence on the conductivity. For example, most 3D MOFs have very low conductivity and produce a large resistance in the conductive channel. This is more suitable for measurements using double-contact technology. The 2D form of MOF conductivity is very high, which is more suitable for measurement by the four-contact method and the Fender wave method. Moreover, in many cases, the electrical conductivity values of MOF materials measured by the same method are different, because different values will be given for MOF materials with different physical forms, such as sheet, polycrystalline film, single-domain film, or single crystals [103,104]. On the other hand, the influence of environmental factors on the conductivity of MOFs cannot be ignored. For example, because MOF materials have a large specific surface area, they can significantly interact with surrounding gases or solvents, resulting in changes in electrical conductivity. Thus, it can be seen that the ideal intrinsic conductivity value is very strict with the environmental conditions and the conditions of the crystal material itself. The ideal criteria for the ideal comparison of conductive MOFs are four-contact measurements of single crystals or van der Wave measurement of single-domain thin films in a vacuum, constant temperature, and darkness [87].

### 3. Application

Since the research and development of conductive MOFs, certain breakthroughs have been made in the design, synthesis, and mechanism research, and many achievements have been made in electrochemistry. The application of conductive MOFs in these fields is briefly summarized in Figure 6.

#### 3.1. Supercapacitor

Unlike batteries, supercapacitors store electric energy in the form of static electricity, which is rapid physical adsorption of oppositely charged ions. This makes it have a high power density and good cycle stability. Therefore, it is a good electrochemical energy storage device. c-MOF can provide a large number of active centers and has excellent pseudo-capacitance. Bao and his colleagues combined transition metals such as Ni<sup>2+</sup> and Cu<sup>2+</sup> with organic ligands (HAB) to construct a 2D c-MOF. This is a high-performance electrode for supercapacitors. The MOF material has a honeycomb-arranged square plane coordination geometry and fine, hierarchical pores. The HAB MOF electrode has a volume

capacitance of up to  $760 \text{ F}\cdot\text{cm}^{-3}$  and a surface capacitance of  $20 \text{ F}\cdot\text{cm}^{-2}$ . Its good cycle stability shows that the capacity can still be maintained at about 90% after 12,000 cycles. Different from MOFs, these MOFs have little change in acidic and alkaline aqueous solutions and have excellent chemical stability [105].

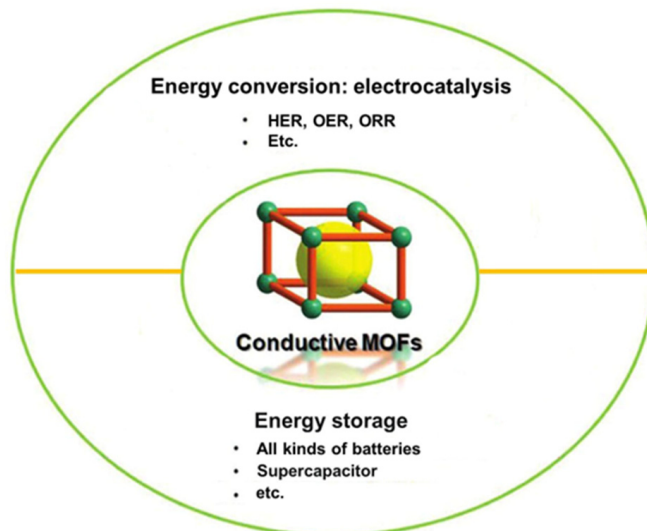


**Figure 6.** Schematic diagram of the applications of conductive MOFs in different fields.

Liu and his team prepared a 3D conjugated metal–organic framework (Cu-DBC) based on divalent copper ions (Figure 7a). The  $\pi$ -d conjugate orbit in its structure makes a large number of delocalized charges exist in the polymer chain, so it has good electrical conductivity. The conductivity of Cu-DBC MOF at room temperature is about  $1.0 \text{ S m}^{-1}$ . They tested this material in nine common solvents and concluded that it is chemically stable. The electrochemical performance of Cu-DBC in 1 M NaCl aqueous solution was tested by a three-electrode system. As shown in Figure 7f, the cyclic voltammetry curves of Cu-DBC in 1 M NaCl solution at different scanning rates show a large, enclosed area and highly reversible REDOX activity, indicating that the capacitance characteristics of Cu-DBC are jointly determined by the EDL capacitance and the Faraday REDOX reaction. The excellent conductivity and REDOX reversibility of the Cu-DBC MOF give it excellent capacitor performance, reaching a weight-specific capacity of  $479 \text{ F}\cdot\text{g}^{-1}$  at a discharge rate of  $0.2 \text{ A}\cdot\text{g}^{-1}$ . The symmetrical solid-state supercapacitor with Cu-DBC as an electrode has an area capacitance of about  $879 \text{ mF}\cdot\text{cm}^{-2}$  and a volume capacitance of about  $22 \text{ F}\cdot\text{cm}^{-3}$ . These data are better than most MOF-based supercapacitors, and Figure 7f summarizes the performance comparison of Cu-DBC and other MOF-based materials for supercapacitors [106]. These data are superior to most MOF-based supercapacitors, showing a good application prospect [107].

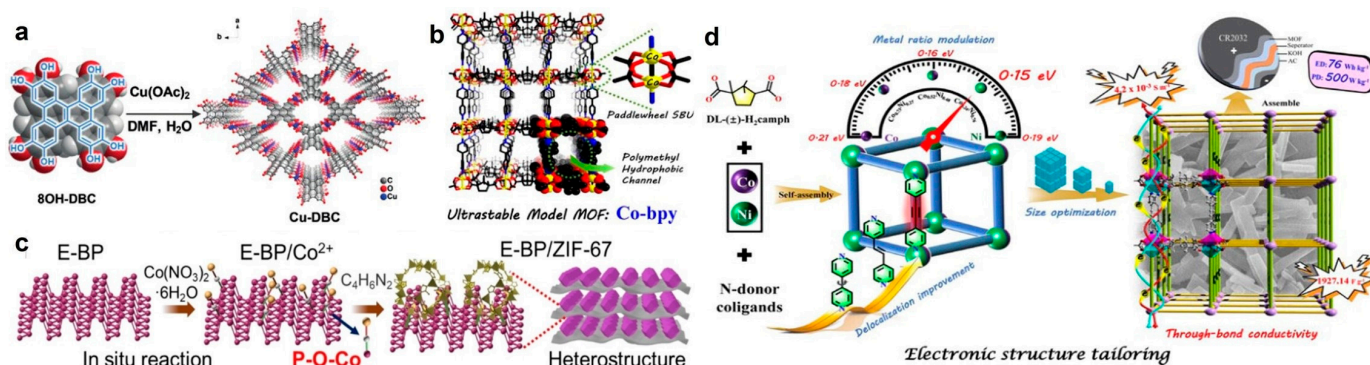


**Figure 7.** Cont.



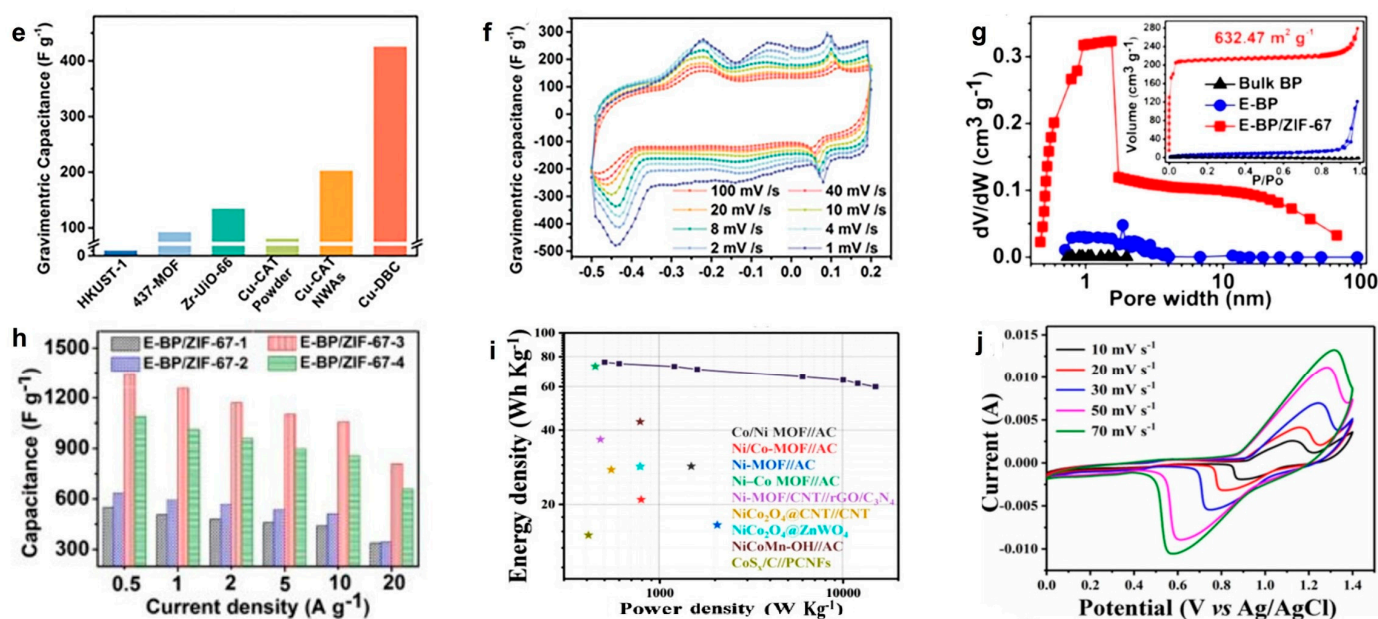


**Figure 7.** (a) Synthesis of Cu-DBC. (b) 3D structural diagram of Co-BPY. (c) Synthetic mechanism of hetero-nano-structured E-BP/ZIF-67. (d) Depiction of the synthesis of the high-performance MOF-based electrode by step-by-step tailoring of the electronic structure of the components. (e) Supercapacitor performance of Cu-DBC in 1 m NaCl. Supercapacitance of Cu-DBC and other MOF-based materials. (f) Supercapacitor performance of Cu-DBC in 1 m NaCl. Cyclic voltammograms profiles at different scan rates. (g) The nano-sized pore distributions of bulk BP, E-BP, and E-BP/ZIF-67. (Inset: typical nitrogen adsorption/desorption isotherms.) (h) The specific capacitances of E-BP/ZIF-67 at different current densities. (i) Electrochemical performance comparison of  $\text{Co}_{0.24}\text{Ni}_{0.76}\text{-bpa-200}/\text{AC}$  and some related asymmetric devices. (j) CV curves at various scan rates. (a,e,f) Reproduced with permission [108]. WILEY-VCH Verlag GmbH & Co. KGaA, Weinheim, 2015. (c,g,h) Reproduced with permission [109]. Wiley-VCH GmbH, 2021. (b,d,j) Reproduced with permission [110]. Wiley-VCH GmbH, 2021).

Wu and his colleagues developed a black-scale/metal-organic skeleton composite containing a P-O-Co covalent bond structure with a large specific surface area of  $632.47 \text{ m}^2 \text{ g}^{-1}$  and a microporosity of  $0.38 \text{ cm}^3 \text{ g}^{-1}$ , whose capacitance reached  $1347 \text{ F} \cdot \text{g}^{-1}$  at  $0.5 \text{ A g}^{-1}$  in a KOH electrolyte. Figure 7c shows the synthesis mechanism of E-BP/ZIF-67 nanostructures. The flexible supercapacitor with this material as an electrode has a high-volume energy density ( $109.8 \text{ mW cm}^{-3}$ ), a large capacitance ( $506 \text{ F} \cdot \text{cm}^{-3}$ ), and maintains good stability after 12,000 cycles. Figure 7g shows the pore distribution and specific surface area of block BP, E-BP, and E-BP/ZIF-67. The micropore characteristics of E-BP/ZIF-67 smaller than 2 nm have been significantly improved. The flexible supercapacitors Wu et al. integrated with the material can provide relatively stable power for some smart devices and can operate for long periods under harsh conditions such as low/high temperatures. Figure 7h shows the general specific capacitance. This work opens up key opportunities for new electrode structural systems and practical applications [111].

Xia and his team prepared a nanoscale MOF with ultra-high stability and semiconductor properties,  $\text{Co}_{0.24}\text{Ni}_{0.76}\text{-bpa-200}$ , which has a specific surface area of  $4.2 \times 10^{-3} \text{ S m}^{-1}$ . The proper positive nickel ions doped in the MOF can reduce the activation energy of the system, increase the concentration of the carrier, and realize effective charge transfer so that MOF has good electrical conductivity. Analysis of the single-crystal structure shows that Co-BPY has a columnar layered three-dimensional structure (Figure 7b). Figure 7d describes the preparation process of the MOF-based material electrode. The picture shows a rich pore structure, which can provide a smooth channel for the diffusion of electrolytes, promote the rapid transmission of electrons, and thus facilitate charge and discharge.

Figure 7j shows the sweep rate in the range 20–70  $\text{mV}\cdot\text{S}^{-1}$  in the potential window of 0–1.4 V. The quasi-rectangular matrix curve coupled with the REDOX peak represents the combined capacitance behavior of the electronic double-layer capacitor and the pseudo capacitor. Due to its unique structure, the cycling stability of  $\text{Co}_{0.24}\text{Ni}_{0.76}\text{-BPA-200MOF}$  remains at about 86.5% after 10,000 cycles [112].

The above research shows that to meet the requirements of supercapacitor application, it is necessary to maintain the structural advantages of MOF while achieving high electrical conductivity and high structural/chemical stability. When designing supercapacitors, it is suggested that the coordination atoms in organic ligands with large atomic sizes and low electron affinity should be selected to obtain a stable MOF structure. In addition, it is advantageous to select metal ions with favorable atomic orbitals in terms of increasing electrical conductivity, as this will affect the orbital overlap between them and the coordination atoms [113]. The properties of common conductive MOFs as electrode materials and their synthesis methods are shown in Table 2.

**Table 2.** Performance of c-MOFs in supercapacitors.

Electrode Materials	Electrolyte	Operating Voltage [V]	Cyclic Stability	Specific Capacitance [ $\text{F}\cdot\text{g}^{-1}$ ]	Electrode Fabrication Method	Ref.
$\text{Ni}_3(\text{HITP})_2$	0.5 M $\text{Na}_2\text{SO}_4$	0–1.00	84% (after 100 000 cycles $0.1 \text{ mAcm}^{-2}$ )	170	electrophoretic deposition	[114]
$\text{CNF@Ni-HITP}$	PVA/KCl gel	0–1.00	90% (after 10 000 cycles $1.0 \text{ Ag}^{-1}$ )	141	neat conductive MOF	[115]
$\text{Cu}_3(\text{HHTP})_2$	1 M $\text{NEt}_4\text{BF}_4/\text{ACN}$	0–1.00	81% (after 30 000 cycles $1.0 \text{ Ag}^{-1}$ )	114	conductive additives and binders	[59]
$\text{Cu-CAT NWAs}$	3 M KCl	−0.40 to 0.50	80% (after 5000 cycles $0.8 \text{ Vs}^{-1}$ )	202	neat conductive MOF	[45]
Ni-HAB	1 M KOH	−0.75 to 0.25	90% (after 12 000 cycles $10.0 \text{ Ag}^{-1}$ )	420	conductive additives and binders	[105]
$\text{Ni}_3(\text{HAB})_2$	0.5 M $\text{Na}_2\text{SO}_4$	0–1.00	81% (after 50 000 cycles $1.0 \text{ mAcm}^{-2}$ )	279	electrophoretic deposition	[116]
Cu-HAB	1 M KOH	−0.55 to 0.10		215	conductive additives and binders	[105]
Co-HAB	1 M $\text{NaPF}_6$	0.50–3.00	100% (after 50 cycles $50.0 \text{ mAg}^{-1}$ )		conductive additives and binders	[49]

### 3.2. Batteries

Supercapacitors and batteries are the two main ways of storing power. Batteries, by contrast, have been the focus of research because of their high energy density. With the development of electronic devices, the power density and energy density of batteries are required to be higher [117]. Figure 8 shows a wide range of applications for batteries, including trolley charging, cell phone charging, wind power generation, and solar power generation, where conductive MOF can also be applied. In this section, we will review the latest progress in the application of c-MOFs in lithium/sodium/zinc batteries.

#### 3.2.1. Lithium-Based Batteries

The lithium battery is a kind of battery with lithium metal or lithium alloy as the positive/negative electrode material and uses a non-aqueous electrolyte. The lithium-ion battery (LIB) is a type of rechargeable battery, which mainly depends on lithium ion moving between the positive and negative terminals for charging and discharging [118]. From the energy storage mechanism of the battery, lithium-ion batteries should use electrode

materials with REDOX activity, and REDOX reactions will occur during the insertion and extraction of lithium ions [119].

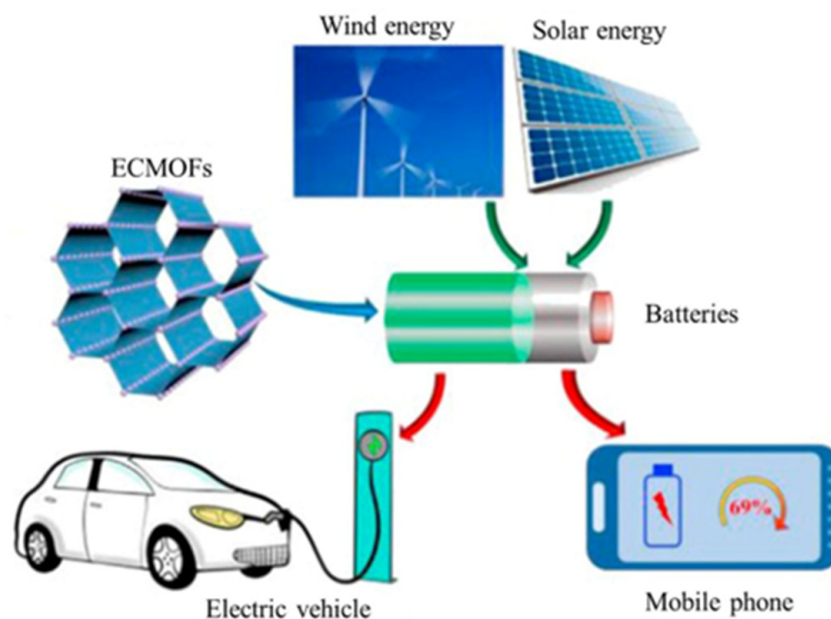


**Figure 8.** The applications of c-MOFs in energy storage devices.

Nishihara et al. reported a metal conducting double (diimide) nickel skeleton (NiDI) prepared with nickel salt and HAB as the nickel source and organic mixture system, which was used as the positive electrode material of a LIB [101]. It has the energy storage principle of both cationic and anionic insertion. The nickel-based c-MOF has a unique unit of REDOX activity,  $\text{Ni}(\text{Lisq})_2$  ( $\text{L} = o$ -diimimylbenzodiaminodiquinate), and its REDOX process includes two electron oxidation and two electron reduction processes, as each metal site has four electron transfers (Figure 9a). The unique intercalation-mediated multielectron transfer characteristics of NiDI are applied to a rechargeable energy storage system. The properties of the material were further investigated in the charge and discharge tests with a current density of  $10\text{--}500 \text{ mA g}^{-1}$  (Figure 9b). The specific capacity depends heavily on the current density. At the current density of  $10 \text{ mA g}^{-1}$ , the specific capacity reaches  $155 \text{ mAh g}^{-1}$ , or the specific energy density of  $434 \text{ Wh kg}^{-1}$ . The cycle performance check at  $250 \text{ mA g}^{-1}$  shows the stable performance of up to 300 cycles (Figure 9c). Through DFT calculation, the estimated state densities of elements near the Fermi level in NiDI show a widely dispersed nature and the characteristics of a non-innocent coordination network reflected by delocalized electrons (Figure 9d).

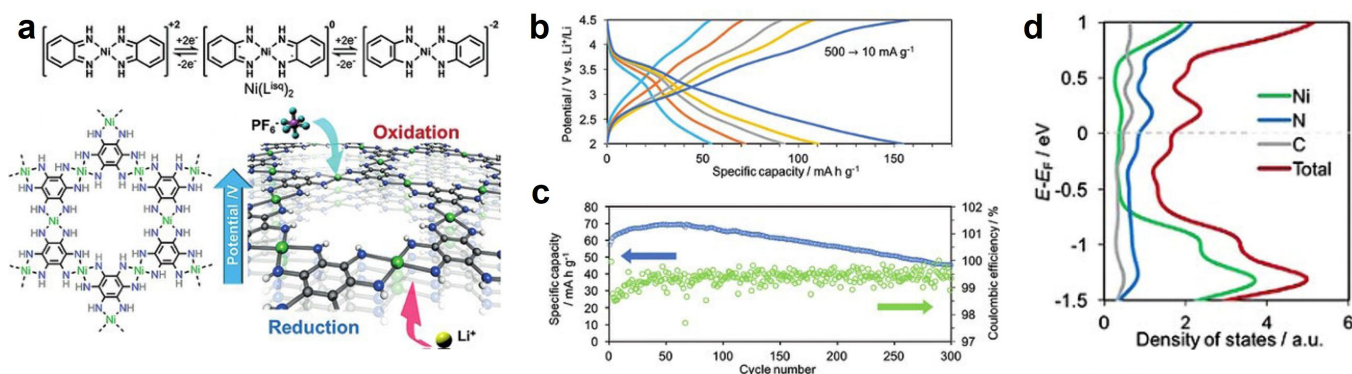


**Figure 9.** Cont.

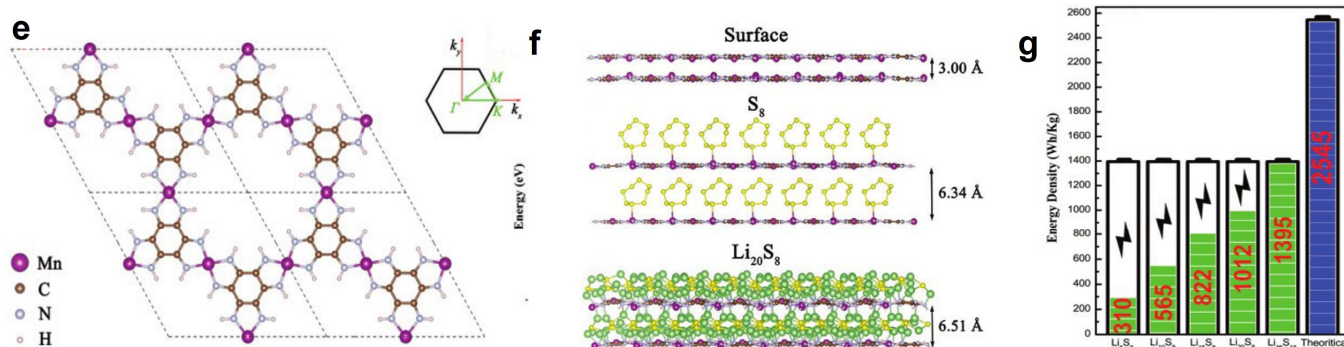


**Figure 9.** (a) Chemical structure and REDOX reaction of  $\text{Ni}(\text{L}^{\text{isq}})_2$  with NiDI. (b) NiDI cathode at  $10\sim 500\text{ mA g}^{-1}$  charge–discharge curve. (c) The NiDI cathode has a cyclic test and Coulomb efficiency up to 300 times at a current density of  $250\text{ mA g}^{-1}$ . (d) NiDI projection state density with AA stacking mode. (e) The geometric structure of the Mn-HAB-CP monolayer is shown. (f) From top to bottom are the layers spacing of Mn-HAB-CP,  $\text{S}_8$  loaded on Mn-HAB-CP, and  $\text{Li}_{20}\text{S}_8$  loaded on Mn-HAB-CP. The green, yellow, and red background colors represent the single, linear, and reticular  $\text{Li}_x\text{S}_y$ , respectively. (g) This represents the energy density of  $\text{Li}_x\text{S}_y$  on Mn-HAB-CP with solvent effect at different physicochemical stages in the range of  $2.0\text{ mA}/4.5\text{ V}$  vs.  $\text{Li}/\text{Li}^+$ , which is one of the highest among the rechargeable batteries. ((a–d) Reproduced with permission [120]. Wiley-VCH Verlag GmbH & Co. KGaA, Weinheim, 2018. (e–g) Reproduced with permission [121]. WILEY-VCH Verlag GmbH & Co. KGaA, Weinheim, 2018.).

Guo and his team designed a scalable bottom-up preparation of a 1D Cu-based c-MOF, Cu-CAT, using solvothermal methods, and used it as a cathode material for lithium-ion batteries. The material exhibits a very high reversible capacity with a magnification of about  $631\text{ mAh g}^{-1}$  at  $0.2\text{ A g}^{-1}$  and about  $381\text{ mAh g}^{-1}$  at  $2\text{ A g}^{-1}$ . The discharge capacity remains at about 81% after 500 cycles at  $0.5\text{ A g}^{-1}$  [122]. Gu and his colleagues explored the synthesis of a new conducting metal–organic skeleton,  $\text{Cu}_3(\text{HHTP})_2$ , and used it as a cathode material for LIBs. The reversible discharge and charging capacity of the  $\text{Cu}_3(\text{HHTP})_2$  cathode is about  $95\text{ mAh g}^{-1}$  in the working voltage range of  $1.7\sim 3.5\text{ V}$ . When used as the cathode of the LIB, the material can maintain stable REDOX cycle performance even at current ratios up to 20 C [123].

Compared with the LIB, the lithium–sulfur battery (LSB) has a higher theoretical specific capacity, low cost, and abundant resource utilization [124]. However, the volume expansion of sulfur and insulation performance will lead to the deterioration of cycle stability and multiplier performance of LIBs [125]. At the same time, the shuttle effect caused by soluble polysulfide in the process of charge–discharge will seriously affect the application of LSBs [126]. The c-MOF has high conductivity and adjustable pore size and is a good material for sulfur carriers. Gao et al. explored and developed a 2D-hexamino phenyl coordination polymer, 2D-HAB-CP, as a candidate material for the cathode of LSBs. Figure 9e shows the structure of 2D-HAB-CP synthesized by the top-down method. The 2D-HAB-CP has two coordinated nitrogen atoms, excellent electrical conductivity, abundant structural pores, and a high proportion of transition metal atoms [127].

### 3.2.2. Sodium-Ion Batteries

Sodium-ion batteries (SIBs) are considered a new generation of energy storage equipment after LIBs because of their wide distribution, low potential, and low cost [93]. The molar mass and ionic radius of sodium ions are larger than those of lithium ions. Although the working principle of SIBs is similar to that of LIBs, the most commonly used lithium-ion electrode materials are not suitable for the insertion and extraction of sodium ions. The large molar mass and ion radius will delay the transmission delay of sodium ions, and the efficiency, tolerance, and energy density of sodium-ion batteries will decrease [108]. Therefore, the electrode material used for SIBs must have a large tunnel size, and REDOX

activity occurs during the insertion and extraction of sodium ions. Compared with inorganic materials and organic materials, c-MOF materials with REDOX activity may be more suitable as electrode materials for secondary sodium-ion batteries, because the combination of metal parts and organic connectors can show higher electron conductivity and structural robustness [109].

Bao and his colleagues prepared a cobalt-based c-MOF (Co-HAB) with high stability and good conductivity [49]. The results show that Co-HAB batteries exhibit a very low self-discharge rate and high area capacitance. Liu et al. reported on SIHC, which was led by the Ministry of Finance metal conduit structure, anode material Cu-CATt, or  $\text{Cu}_3\text{HHTP}_2$  [128]. The results show that the reversible capacity of the prepared Cu-CAT nanowires loaded on nickel foam as a negative electrode is  $260 \text{ mAh g}^{-1}$  at the current density of  $0.1 \text{ A g}^{-1}$ . The results show that the anode of Cu-CAT nanowires stores sodium ions through coordination with oxygen atoms in the carbon–oxygen bond and associated reduction of copper ions. Feng and his team reported in 2019 a perfectly conjugated cupric phthalocyanine-MOF, M2-O8-PcCu sodium–iodine cell using iodine as a positive electrode material [129]. Fe2-O8-PcCu/I2 shows excellent cycle durability after atomic level modulation, and the specific capacity of Fe2-O8-PcCu /I2 reaches  $150 \text{ mAh g}^{-1}$  after 3000 cycles. There are many Fe-O4 planar nodes in the network frame of Fe2-O8-PcCu, which can bond poly iodine and inhibit its solution in the nation, which is one of the keys to improving its cycling durability.

The organic part and the metal part of the c-MOF system have considerable chemical adjustability. The application of the c-MOF sodium-ion series is still in its infancy, so it is necessary to further explore the basic knowledge of the electrochemical process and reaction principle, to provide effective guidance for the design of c-MOFs which can be applied in sodium-ion batteries.

### 3.2.3. Zinc-Based Batteries

A rechargeable zinc-based battery is a kind of water-based battery with high safety and relatively low cost. Compared with lithium and sodium batteries, it effectively reduces the safety risk of leakage and combustion of organic electrolytes. Zinc-based batteries usually use zinc as the negative electrode and use hydrolyses, which makes the rechargeable zinc-based batteries have the advantages of low cost, high safety, and high theoretical capacity [110]. Compared with the lithium battery and sodium battery, the zinc water-based battery has remarkable rate performance and upper power density because of the excellent ionic conductivity of the electrolyte in water. In addition, due to the small ion radius of zinc ions, the c-MOF has open channels and rich REDOX activity during the insertion and extraction of zinc ions and can be used as zinc-ion battery cathode material [130].

Yao and his team developed a novel self-sacrificing synthesis method in 2019 by self-sacrificing synthesis of conductive vanad-based three-dimensional nano harness arrays (V-EC-MOF) on carbon nanotube fibers to be used as binder-free positive electrodes for zinc-ion batteries [131]. Figure 10a shows a self-sacrificing synthesis route for generating a layered 3D V-MOF nano harness array on the surface of CNTF. The compound has abundant active centers, layered porosity, and high conductivity. Figure 10c shows the magnification capacity of zinc-ion batteries at different current densities. V-MOF-48//zinc current density increased by 50 times to 64.3% of the initial capacity and V-MOF-24//zinc current density increased by 50 times to 56.1% of the initial capacity, both of which show excellent multiplier performance. However, V-MOF-12//zinc and VMF-60//zinc only maintain 42.9% and 39.7% of the initial capacity when the current density increases 16 times and 50 times, respectively, which is inferior to the former. The unique 3D multi-channel hierarchical structure greatly shortens ion diffusion distances and increases ion transport rates, thus enhancing rate capability, which is critical for practical applications. Figure 10d is an all-solid fibrous V-MOF-48//zinc cell assembled with PVA electrolyte. The practical applicability of the cell was evaluated using the Ragone diagram. The results showed good electrochemical stability with an initial capacitance of 81.5% at 300 cycles with a current density of  $2.0 \text{ A cm}^{-3}$ .

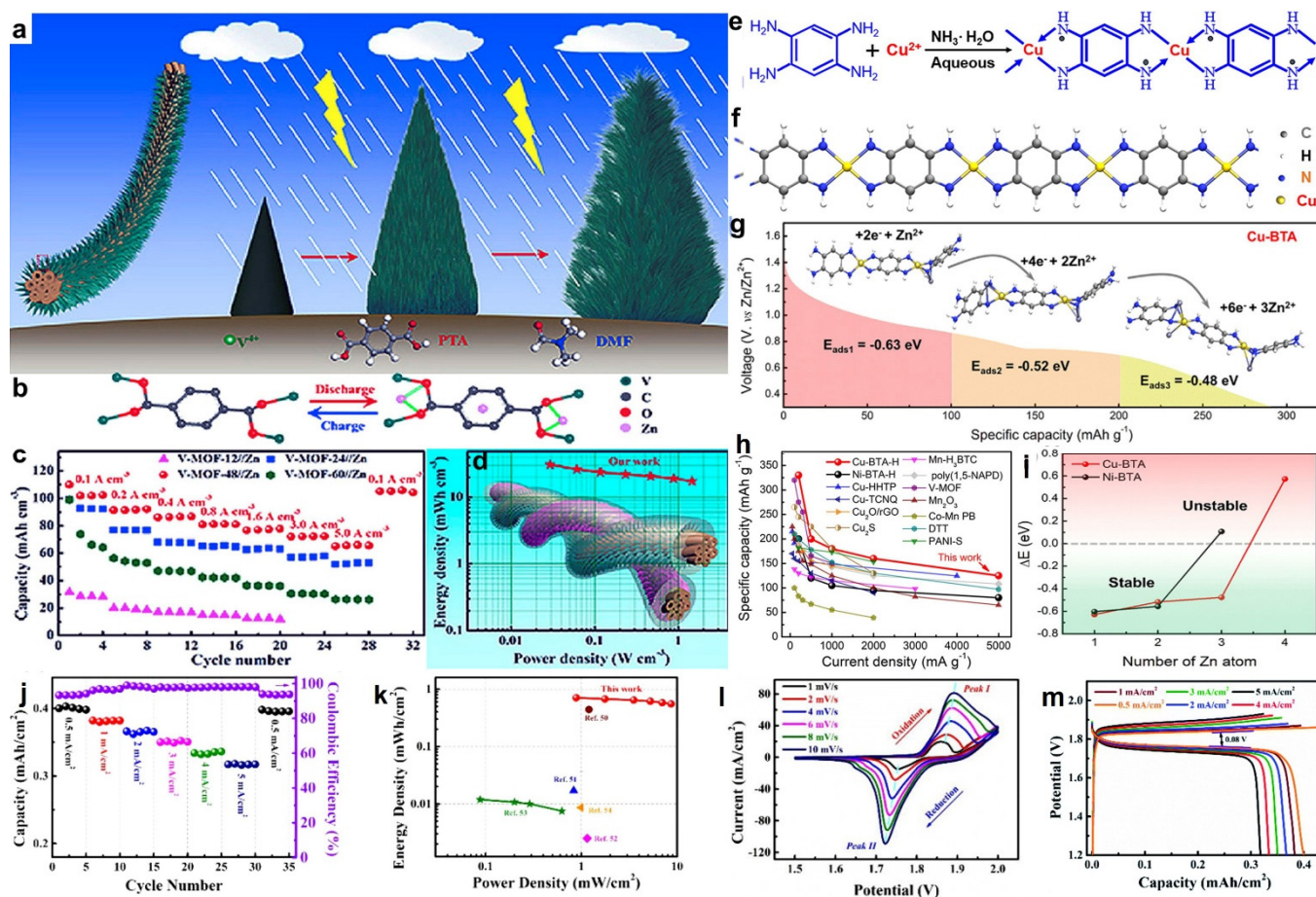


**Figure 10.** (a) Schematic diagram of the preparation process of V-MOF@CNTF with a hierarchical nanowire structure. (b) Possible zinc binding site with V-MOF-48@CNTF coordination. (c) Specific capacities of V-MOF-12//zinc, V-MOF-24//zinc, V-MOF-48//zinc, and V-MOF-60//zinc at different current densities. (d) Schematic diagram of an all-solid-state fibrous V-MOF-48//zinc battery. (e) Schematic diagram of the Cu-BTA synthesis process. (f) An overview of the molecular structure of one-dimensional planar conjugated Cu-BTA. (g) Structure evolution and protonation path of Cu-BTA during discharge. (h) Comparison of Copper-BTA-H with other ZIB cathodes, including: Cu-HHTP, 26 Cu-TCNQ, 31 Cu<sub>2</sub>O/rGO, 32 Cu<sub>2</sub>S, 33 Mn-H<sub>3</sub>BTC, 34 poly(1,5-NAPD), 35V-MOF, 36 Mn<sub>2</sub>O<sub>3</sub>, 37 Co/Mn-PB, 38 DTT, 39, and PANI-S. (i) The sequential binding energy of Cu-BTA/Ni-BTA with different zinc ion loads. (j) The production of FAR nickel–zinc battery schematic diagram and section diagram. (k) The energy power density of the prepared nickel–zinc battery was compared with that of the silver–zinc battery 46, graphene supercapacitor 47, manganese dioxide supercapacitor 48, nickel–zinc battery 49, and graphene fiber micro-supercapacitor 50. (l) Magnification capacity and Coulomb efficiency of Ni-MOF/CNTF. (m) Cyclic voltammetry curves of Ni-MOF/CNTF at different scanning rates of 1–10 mV/s. ((a–d) Reproduced with permission [132]. Published by Elsevier Ltd., 2019. (e–i) Reproduced with permission [90]. American Chemical Society, 2023. (j–m) Reproduced with permission [133]. Royal Society of Chemistry, 2020.).

Stoddart et al. applied 2DMOF Cu<sub>3</sub>HHTP<sub>2</sub> to the zinc cell cathode with 1D channel and REDOX activity  $\pi$ -conjugated conduction [44]. The results show that Cu<sub>3</sub>HHTP<sub>2</sub> has good cyclic stability, with a capacity retention rate of 75% after 500 cycles and a reversible capacity of up to 228 mAh g<sup>-1</sup> at 50 mA g<sup>-1</sup>. Li and his colleagues directly synthesized Ni-PTA-Mn, a metal–organic skeleton porous material with a large specific surface area and electrical conductivity, using a one-step hydrothermal method [79]. When it is used as the positive electrode of a water-based zinc-ion battery, the specific discharge capacity of the battery at 0.1 A g<sup>-1</sup> can reach 139 mA g<sup>-1</sup>, 1 A g<sup>-1</sup>, and the capacity retention rate is

about 93% after 100 cycles. The excellent electrochemical performance is determined by the proton conductivity of the metal–organic skeleton hydrogen bond network.

Sang and his colleagues obtained a highly crystalline  $\pi$ -d-conjugated conductive metal–organic skeleton by coordinating the ultra-small 1, 2, 4, 5-phenyltetramine (BTA) ligand with copper ions (Cu-BTA-H) (Figure 10e), which can be used as the positive electrode material of zinc water-based batteries [134]. The compound has a one-dimensional (1D) Cu-BTA chain with a  $\pi$ - $\pi$ / $\pi$ -d conjugate structure with abundant delocalized electrons (Figure 10f). The results show that the reversible capacity of the cathode material is 330 mAh g<sup>-1</sup> at 200 mA g<sup>-1</sup>, which shows excellent magnification performance and long cycle stability. After 500 cycles, the capacity is 106.1 mAh g<sup>-1</sup> at 2.0 A g<sup>-1</sup>, and the Coulomb efficiency is ~100%. The proposed c-MOF with a double REDOX active center provides an effective method for the construction of fast, stable, and large-capacity energy storage devices. Stoddart's team is the first to use a conductive metal–organic skeleton (Cu<sub>3</sub>(HHTP)<sub>2</sub>) as a cathode for a zinc-ion battery [44]. Cu<sub>3</sub>(HHTP)<sub>2</sub> has very high conductivity and zinc ions can migrate rapidly in the Cu<sub>3</sub>(HHTP)<sub>2</sub> structure with minimal volume change during repeated ion insertion extraction. Due to the existence of these characteristics, Cu<sub>3</sub>(HHTP)<sub>2</sub> can obtain high reversible capacity and multiplier ability.

Compared with the zinc-ion battery, the zinc–nickel battery has a higher specific capacity, lower cost, relatively abundant resources, and relatively high operating voltage [135]. Yao et al. applied a nickel-based c-MOF nanosheet array directly grown on carbon nanotubes which will be applied to the cathode of a high-voltage nickel–zinc cell in a fibrous form in 2020 [136]. The results show that the nickel–zinc battery has good conductivity, unique structure, and can show good stability, and the initial capacity retention rate is still 89% after 600 cycles. The successful application of the nickel–zinc battery provides a new idea for the rational design of c-MOFs in the next generation of wearable electronic devices. Although this is a successful attempt, the problems of low energy density and poor cycle performance still exist. The reason is that the metal part of c-MOF plays a decisive role in the REDOX center of Ni-MOF. C-MOF is less stable in alkaline solution. The operating voltage of conducting MOFs in experiments is low, which limits the application of conducting MOFs in zinc-ion batteries. Therefore, it is necessary to further explore the strategy of improving the working voltage of the MOF-based conducting zinc batteries. Table 3 summarizes the charge–discharge capacity and cycle stability of different electrode materials and their synthesis methods in batteries. The performance of common conductive MOFs in different batteries and their synthesis methods are shown in Table 3.

**Table 3.** Properties and synthesis methods of conductive MOFs in different batteries.

Electrode Material	Charge and Discharge Capacity	Cyclic Stability	Synthesis Method	Apply	Ref.
Cu-CAT	631 mAhg <sup>-1</sup>	81%	Solvothermal method	Lithium-ion battery	[122]
Cu <sub>3</sub> (HHTP) <sub>2</sub>	95 mAHg <sup>-1</sup>		Solvothermal method	Lithium-ion battery	[123]
Co-HAB	260 mA h g <sup>-1</sup>		Solvothermal method	Sodium-ion battery	[131]
V-EC-MOF		81.5%	Solvothermal method	Zinc-ion battery	[134]
Cu <sub>3</sub> HHTP <sub>2</sub>	228 mAh <sup>-1</sup>	75%	Solvothermal method	Zinc-ion battery	[136]
Cu-BTa-H	330 mAh <sup>-1</sup>	32%	Solvothermal method	Zinc-ion battery	[135]
Ni-MOF/CNTF	0.4 mA h cm <sup>-2</sup>	600%	Water bath method	Nickel–zinc battery	[120]

### 3.3. Electrocatalysis

Electrochemical energy conversion technology is a kind of clean and renewable energy storage technology [47,137]. C-MOF with REDOX ligands and metal junctions is considered an ideal energy conversion electrocatalyst. Its advantages include: (1) the high conductivity of intrinsic electrons which promotes charge transfer; (2) structural plasticity defines the catalytic location; (3) the large surface area and the adjustable porosity promote the diffusion of electrolytes co-catalyze guest active materials as host materials.

Nishihara and his team prepared a new c-MOF (NiAT), which consists of nickel nodes and a single layer of 1,3,5-aminophenyl-2,4,6-tri mercaptan [47]. The double nickel unit of the c-MOF can be transformed into its double nickel structure by a proton-coupled REDOX reaction, and the conductivity increases from  $3 \times 10^{-6}$  to  $1 \times 10^{-1} \text{ S}\cdot\text{cm}^{-1}$ . Huang and his colleagues designed and synthesized a c-MOF with high conductivity, Cu-BHT, which generally maintains a conductivity of around  $103 \text{ S}\cdot\text{cm}^{-1}$  [138]. As shown in Figure 11a, thin films, nanocrystals, and nanoparticles of Cu-BHT were obtained through different synthesis procedures. The experimental results show that Cu-BHT exhibits good activity and stability under acidic conditions and high current density, and it is a very promising electrocatalytic candidate material. Under the optimized conditions, the slope of Tafel is about  $\sim 95 \text{ mV}\cdot\text{dec}^{-1}$  and the exchange current density is  $10^{-3} \text{ mA}\cdot\text{cm}^{-2}$ . Durability is an important index to measure in a HER catalyst. Huang et al. evaluated the long-term durability of NP-1 by performing 2000 cycle scans in a buffer solution with a pH of 0, ranging from 0–0.75 V. After cycling, the catalyst showed a polarization curve similar to that of the initial test (Figure 11b), indicating that the catalytic performance of NP-1 remained appropriate. The illustrations show that the NP-1-modified GCE can operate at a current density of  $\sim 260 \text{ mA}\cdot\text{cm}^{-2}$ , and in a highly acidic solution of  $-0.7 \text{ V}$ , it can operate continuously for more than 20 h with little loss. At an overpotential of 600 mV, the impedance of the GCE/Np-1 electrode ( $110 \Omega$ ) is much lower than that of the GCE/NC-1 electrode ( $1300 \Omega$ ) (Figure 11c).

The morphology and properties of Cu-BHT in sulfuric acid show that, compared with thin films and nanocrystals, the morphology of nanoparticles greatly reduces the overpotential of oxygen evolution (OER). OER is a clean, reliable, and renewable energy system of the core process; it occurs in the water decomposition process and the metal–air batteries [121,139]. It is worth noting that a large number of proton-coupled electron transfer and polyphase reaction processes involved in the OER process hinder the further development of high-performance electrocatalysts [140,141]. High conductivity, abundant active centers, and faster interfacial reactions are required for high-performance OER electrocatalysts. Therefore, c-MOF with excellent pore structure and intrinsic conductivity becomes a candidate material for an OER electrocatalyst. Peng et al. used copper foam as a base to prepare copper hydroxide nanowires, and then synthesized 2D c-MOF( $\text{Cu}_3\text{HITP}_2$ ) by in situ synthesis and used it as a bifunctional electrocatalyst [142]. The results show that  $\text{Cu}_3\text{HITP}_2$  prepared from copper hydroxide nanowires has a large electrochemical specific surface area and can operate stably in 0.1 and  $1.0 \text{ mol}\cdot\text{L}^{-1}$  KOH solutions. When the current density reaches  $10 \text{ mA}\cdot\text{cm}^{-2}$ , the OER overpotential is only 1.53 V, which is superior to the catalytic performance of commercial catalysts. Huang and his colleagues reported a  $\pi$ -d-conjugated 2D  $\text{Co}_3(\text{HITP})_2$  with a good porous network and abundant oxygen evolution active centers [143]. They synthesized  $\text{Co}_3(\text{HITP})_2$  using a simple method at room temperature (Figure 11d).  $\text{Co}_3(\text{HITP})_2$  shows better conductivity than hole graphene, generally around  $1150 \text{ S}\cdot\text{m}^{-1}$ . The results showed that  $\text{Co}_3(\text{HITP})_2$  showed significant oxygen evolution activity in alkaline electrolytes. Figure 11e shows the timing potential curve of  $\text{Co}_3(\text{HITP})_2$ . The illustration shows the polarization curve of  $\text{Co}_3(\text{HITP})_2$  after 2000 cycles. Additionally, when the current density is  $10 \text{ mA}\cdot\text{cm}^{-2}$ , the overpotential is 254 mV, which is better than most cobalt-based materials and commercial catalysts reported to date. By the density functional theory calculation, it is shown that  $\text{Co}_3(\text{HITP})_2$  has high electron conductivity. The Tafel slope of  $\text{Co}_3(\text{HITP})_2$  is  $86.5 \text{ mV dec}^{-1}$ , much lower than that of HITP ( $530.3 \text{ mVdec}^{-1}$ ), and similar to that of  $\text{IrO}_2$  ( $61.4 \text{ mVdec}^{-1}$ ) and  $\text{RuO}_2$  ( $69.1 \text{ mVdec}^{-1}$ ). It is shown that  $\text{Co}_3(\text{HITP})_2$  has better catalytic kinetics for OER (Figure 11f). It is a new way to develop highly efficient OER electrocatalysts to regulate the electronic structure by the flexible structure of 2D conducting conjugated MOFs. Zhao and his team designed and synthesized an array of NiFe-MOF ultrathin nanosheets grown on nickel foam [144]. The material is prepared by adding organic ligands to a metallic brine solution by a simple one-step chemical bath deposition method. As shown in Figure 11g, the crystal structure of MOF consists of alternating layers of organic hydrocarbons and



inorganic metallic oxygen. This material has graded porosity, good conductivity, and abundant active metal sites, and at  $10 \text{ mA}\cdot\text{cm}^{-2}$ , the overpotential is 240 mV, 0.1 M KOH (Figure 11h). It was the smallest of all the control samples. The Tafel map obtained from the linear sweep voltammetry (LSV) (Figure 11i) shows that the NiFe-MOF electrode has a higher OER efficiency than other laboratories; when it is used as an anode or cathode catalyst, HER also shows considerable activity. The device provides only 1.55 V at  $10 \text{ mA}\cdot\text{cm}^{-2}$ , which is better than the platinum/carbon cathode materials and IrO<sub>2</sub> anode materials used commercially. Wang and his colleagues reported a c-MOF nanowire array grown on carbon cloth as an electrocatalyst for OER [145]. They were able to grow Ni-HHTP nanocrystals directly onto the carbon cloth by immersing it in a reaction solution. The prepared Ni-HHTP nanocrystalline structure consisted of two different types of alternating accumulation layers (Figure 11m,n). The OER activity of nanowire arrays at 1 M KOH (pH = 14) was measured by LSV. As shown in Figure 11l, the Ni-HHTP nanowire array obtains a current density of  $10 \text{ mA}\cdot\text{cm}^{-2}$  at 1.61 V, corresponding to an overpotential of ~380 mV. The slope of the Tafel diagram (Figure 11k) of Ni-HHTP is  $106 \text{ mV dec}^{-1}$ . When Fe is doped, the slope drops to  $96 \text{ mV dec}^{-1}$ , reflecting the enhancement of electrochemical kinetics and the transfer of the rate-determining step from M-OH to M-O. It relies on the principle that non-cracking c-MOF electrocatalysts can preserve the original intrinsic molecular active center in MOFs. The overpotential of the prepared electrodes was ~213 and 300 mV at  $10 \text{ mA}\cdot\text{cm}^{-2}$  and  $150 \text{ mA}\cdot\text{cm}^{-2}$ , respectively, which showed long-term stability in 1 M KOH. Du et al. successfully synthesized a 2D c-MOF, NiPC-MOF, using a top-down preparation method for high-efficiency water oxidation catalysis [146]. Figure 11j shows the synthesis and chemical structure of the NiPC-MOF material. It has excellent catalytic activity against OER. The NiPC-MOF films grown on FTO were designed and showed very low initial potential and overpotential of 0.25 V, good catalytic stability, and mass activity.

At present, the main electrocatalyst of ORR is platinum group metals [90,132,133,147]. However, due to its high cost, poor stability, poor safety, and other problems, its commercial application in fuel cells is limited. Due to this, the preparation of new c-MOFs using non-platinum group metals as electrocatalysts emerged. Oh and his colleagues report that a bimetallic conducting MOF, Co<sub>x</sub>Ni<sub>y</sub>-CAT, which has two metal ions (cobalt and nickel) that are free to adjust the ratio, is a suitable electrocatalyst for ORR [148]. Compared with mono-metal Co<sub>x</sub>Ni<sub>y</sub>-CAT or Ni-CAT, bimetallic Co<sub>x</sub>Ni<sub>y</sub>-CAT has better ORR properties, exhibits an ideal four-electron transfer pathway, and lower hydrogen peroxide release degree. In the ORR process, bimetallic Co<sub>x</sub>Ni<sub>y</sub>-CAT retains the high diffusion limit current density advantage of Co-CAT and the high initial potential advantage of Ni-CAT. Feng and his team developed a phthalate group MOF conductor, PcCuO<sub>8</sub>-CO, as a high-performance ORR catalyst [149]. After compositing with carbon nanotubes, this compound has a very high ORR activity active Co-O<sub>4</sub> node, unique conductivity, and weekly interval. When the prepared PcCuO<sub>8</sub>-Co is used as the positive electrocatalyst of zinc-air cells, the power density is up to  $94 \text{ mW}\cdot\text{cm}^{-2}$ , and the performance is better than that of the best platinum/carbon electrodes.

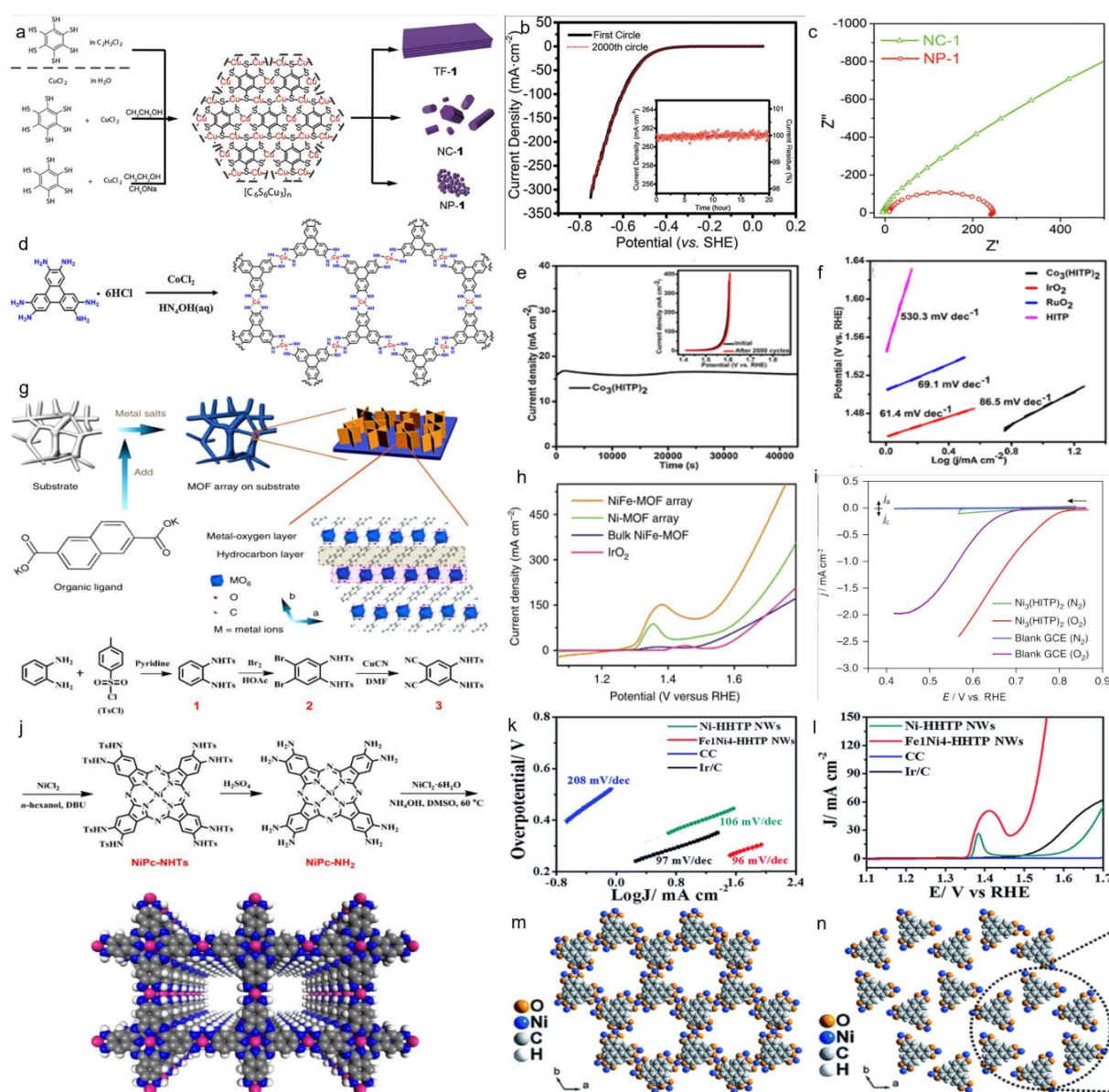


**Figure 11.** (a) Three methods for synthesizing Cu-BHT with corresponding morphology. (b) Durability test: the black line represents the first cyclic voltammogram curve of GCE/NP-1 in 0.5 M H<sub>2</sub>SO<sub>4</sub> solution at a scanning speed of 100 mV/s, and the red line represents the 2000th lap. The illustration is the time dependence of the current density of GCE/NP-1 at a static overpotential of 700 mV. (c) The electrochemical impedance spectra of GCE/NC-1 (green line) and GCE/NP-1 (red line) at the same overpotential in the range of ~10 MHz were compared. (d) Structure and synthesis of Co<sub>3</sub>(HITP)<sub>2</sub>. (e) The timing potential curve of Co<sub>3</sub>(HITP)<sub>2</sub>. The illustration shows the polarization curve of Co<sub>3</sub>(HITP)<sub>2</sub> after 2000 cycles. (f) Tafel comparison of Co<sub>3</sub>(HITP)<sub>2</sub>, HITP, IrO<sub>2</sub>, and RuO<sub>2</sub>. (g) Synthesis of metal–organic skeleton nanosheet arrays. (h) LSV curves of NiFe-MOF, Ni-MOF, block NiFe-MOF, and IrO<sub>2</sub> at 10 MVS<sup>-1</sup> and 0.1 M KOH. (i) Comparison of Tafel of NiFe-MOF, Ni-MOF, and block NiFe-MOF. (j) Structure and chemical synthesis of NiPC-MOF. (k,l) LSV curves and Tafel diagrams of Ni-HHTP NWS, Fe<sub>1</sub>Ni<sub>4</sub>HHTP NWS, carbon cloth (CC), and Ir/C in 1M KOH alkaline solution. (m) Space-filling diagram of Ni-HHTP wrapper structure along the c direction. (Blue for nickel, orange for oxygen, gray for carbon, and light gray for hydrogen). (n) Fill in the diagram for the discrete layer space. ((a–c) Reproduced with permission [150]. American Chemical Society, 2017. (d–f) Reproduced with permission [151]. Elsevier B.V., 2020. (g–i) Reproduced with permission [149]. The Author(s), 2017. (j–n) Reproduced with permission [152]. The Royal Society of Chemistry, 2019.).

The molecular structure of carbon dioxide is very stable, which is a relatively difficult challenge for CRR [153]. Given this, it is very advantageous to develop high-activity CRR electrocatalysts. Therefore, it is of great significance to design a highly designable c-MOF as a promising candidate electrocatalyst [150].

Copper is a very attractive metal that converts carbon dioxide directly into alcohols or hydrocarbons [154]. Gu et al. reported the conductive metal oxide  $\text{Cu}_2(\text{CuTCPP})$  of Cu-based porphyrins, could be used as an electrocatalyst for CRR. The results show that  $\text{Cu}_2(\text{CuTCPP})$  has remarkable catalytic activity on the products of carbon dioxide conversion, and the reaction efficiency is 68.4% at about 1.55 V to Ag/Ag tower potential. This work also shows that the c-MOF has high selectivity and good stability. Table 4 summarizes the overpotential of different electrode materials and their synthesis methods.

**Table 4.** Properties and synthesis methods of conductive MOFs in different catalytic modes.

Electrode Material	Overpotential	Synthesis Method	Apply	Ref.
NIAT		Water bath method	HER catalyst	[139]
Cu-BHT	95 mV	Water bath method	HER catalyst	[121]
$\text{Cu}_3\text{HITP}_2$	1.53 V	Solvothermal method	OER catalyst	[144]
$\text{Co}_3(\text{HITP})_2$	254 mV	Solvothermal method	OER catalyst	[146]
NiFe-MOF	240 mV	Solvothermal method	HER catalyst	[147]
Ni-HHTP nanowire array	~380 mV	Solid-liquid interface method	OER catalyst	[132]
NiPC-MOF	0.25 V	A top-down method for preparing efficient water oxidation catalysts	OER catalyst	[90]
$\text{Co}_x\text{Ni}_y\text{-CAT}$		Hydrothermal method	ORR catalyst	[154]
$\text{PcCuO}_8\text{-CO}$		Hydrothermal method	ORR catalyst	[149]
$\text{Cu}_2(\text{CuTCPP})$	1.55 V	Solvothermal method	CRR catalyst	[155]

#### 4. Conclusions and Outlook

During the past twenty years, MOFs, as important multifunctional materials, have been widely concerned and developed rapidly [156]. Up to now, more than 20,000 different MOFs have been reported, which are flexible in structure and diverse in chemical composition. The MOF's ultra-high porosity, specific surface area, adjustable functionality, and impressive thermal and chemical stability make it an excellent candidate for diverse related energy applications. Conducting MOF materials can make good charge transport and high porosity coexist, which is conducive to the development of the next generation of energy technology [157].

To sum up, giving electrical conductivity to MOFs is to incorporate traditional MOFs into the field of conducting MOFs and to expand their electrochemical applications [158]. In this paper, we explored the synthesis of c-MOF, the design strategy of c-MOF electrodes, and the latest progress of c-MOF in supercapacitors, lithium/sodium/zinc batteries, or HRR/ORR, etc. [151]. Although many achievements have been made, the research on c-MOF is still in the preliminary stage. Several deficiencies and defects of c-MOF are summarized as follows:

1. The application of c-MOF in electrocatalysts is a hot topic in the field. At present, however, its performance cannot be compared with that of precious metal catalysts [152];
2. It is important to explain the relationship between the active center of c-MOF and the potential generated by the electrode during ion insertion and extraction [159];
3. To obtain better ion storage capacity of charge transfer, the structure of c-MOF needs to be adjusted accurately [160–166].

Given this, environmentally friendly and high-performance electrochemical devices based on conducting MOFs will become the focus of future research [3]. In the future, with the close collaboration of experimenters, theorists, and computational chemists in this field, c-MOFs are expected to make a breakthrough as the next generation of functional materials [167–170].

To sum up, conductive MOFs have unique properties and show great application potentials in energy storage and conversion. The development of MOFs has opened up an entirely new way for the scientific application of porous materials, and making MOFs electrically conductive so that they can be used as electrodes has become an urgent task in the past decade. However, further in-depth and systematic study of the above challenges and progress, as well as long-term research and application, are the inevitable requirements for conducting MOF research to move from the laboratory to industrial production [171–174].

**Author Contributions:** Writing—original draft preparation, M.L.; writing—review and editing, G.Z., Y.S., H.Z., Y.Z. and H.P. All authors have read and agreed to the published version of the manuscript.

**Funding:** This work was supported by the National Natural Science Foundation of China (U1904215), the Natural Science Foundation of Jiangsu Province (BK20200044), and the Changjiang Scholars program of the Ministry of Education (Q2018270).

**Data Availability Statement:** Data available in a publicly accessible repository. The data presented in this study are openly available.

**Acknowledgments:** We thank Huan Pang, Yongcai Zhang, Guangxun Zhang, Yuxin Shi, and Huijie Zhou for their help with this work.

**Conflicts of Interest:** The authors declare no conflict of interest.

## References

1. Ze-Hui, L.; Mei-Juan, T.; Yuan-Hao, Z.; Yu-Yang, L.; Qiu-Shi, J.; Ming-Jie, L. Application of Conductive Metal Organic Frameworks in Supercapacitors. *J. Inorg. Mater.* **2020**, *35*, 433–780. [[CrossRef](#)]
2. Choi, C.; Ashby, D.S.; Butts, D.M.; DeBlock, R.H.; Wei, Q.; Lau, J.; Dunn, B. Achieving High Energy Density and High Power Density with Pseudocapacitive Materials. *Nat. Rev. Mater.* **2019**, *5*, 5–19. [[CrossRef](#)]
3. Gund, G.S.; Dubal, D.P.; Patil, B.H.; Shinde, S.S.; Lokhande, C.D. Enhanced Activity of Chemically Synthesized Hybrid Graphene oxide/Mn<sub>3</sub>O<sub>4</sub> Composite for high Performance Supercapacitors. *Electrochimica Acta* **2013**, *92*, 205–215. [[CrossRef](#)]
4. Dubal, D.P.; Kim, J.G.; Kim, Y.; Holze, R.; Kim, W.B. Demonstrating the Highest Supercapacitive Performance of Branched MnO<sub>2</sub> Nanorods Grown Directly on Flexible Substrates using Controlled Chemistry at Ambient Temperature. *Energy Technol.* **2013**, *1*, 125–130. [[CrossRef](#)]
5. Dubal, D.P.; Holze, R. Self-Assembly of Stacked Layers of Mn<sub>3</sub>O<sub>4</sub> Nanosheets Using a Scalable Chemical Strategy for Enhanced, Flexible, Electrochemical Energy Storage. *J. Power Sources* **2013**, *238*, 274–282. [[CrossRef](#)]
6. Snook, G.A.; Kao, P.; Best, A.S. Conducting-Polymer-Based Supercapacitor Devices and Electrodes. *J. Power Sources* **2011**, *196*, 1–12. [[CrossRef](#)]
7. Ramya, R.; Sivasubramanian, R.; Sangaranarayanan, M. Conducting Polymers-Based Electrochemical Supercapacitors—Progress and Prospects. *Electrochim. Acta* **2013**, *101*, 109–129. [[CrossRef](#)]
8. Wang, Y.; Foo, C.Y.; Hoo, T.K.; Ng, M.; Lin, J. Designed Smart System of the Sandwiched and Concentric Architecture of RuO<sub>2</sub>/C/RuO<sub>2</sub> for High Performance in Electrochemical Energy Storage. *Chem. A Eur. J.* **2010**, *16*, 3598–3603. [[CrossRef](#)]
9. Wang, D.-W.; Li, F.; Liu, M.; Lu, G.Q.; Cheng, H.-M. 3D Aperiodic Hierarchical Porous Graphitic Carbon Material for High-Rate Electrochemical Capacitive Energy Storage. *Angew. Chem. Int. Ed.* **2008**, *47*, 373–376. [[CrossRef](#)]
10. Zhang, L.L.; Zhao, X.S. Carbon-based materials as supercapacitor electrodes. *Chem. Soc. Rev.* **2009**, *38*, 2520–2531. [[CrossRef](#)]
11. Salunkhe, R.R.; Kaneti, Y.V.; Yamauchi, Y. Metal–Organic Framework-Derived Nanoporous Metal Oxides toward Supercapacitor Applications: Progress and Prospects. *ACS Nano* **2017**, *11*, 5293–5308. [[CrossRef](#)] [[PubMed](#)]
12. Luo, S.; Zhao, J.; Zou, J.; He, Z.; Xu, C.; Liu, F.; Huang, Y.; Dong, L.; Wang, L.; Zhang, H. Self-Standing Polypyrrole/Black Phosphorus Laminated Film: Promising Electrode for Flexible Supercapacitor with Enhanced Capacitance and Cycling Stability. *ACS Appl. Mater. Interfaces* **2018**, *10*, 3538–3548. [[CrossRef](#)] [[PubMed](#)]
13. Guo, X.; Bai, N.; Tian, Y.; Gai, L. Free-Standing Reduced Graphene Oxide/Polypyrrole Films with Enhanced Electrochemical Performance for Flexible Supercapacitors. *J. Power Sources* **2018**, *408*, 51–57. [[CrossRef](#)]
14. Wang, X.; Mathis, T.S.; Li, K.; Lin, Z.; Vlcek, L.; Torita, T.; Osti, N.C.; Hatter, C.; Urbankowski, P.; Sarycheva, A.; et al. Influences from Solvents on Charge Storage in Titanium Carbide MXenes. *Nat. Energy* **2019**, *4*, 241–248. [[CrossRef](#)]
15. Augustyn, V.; Simon, P.; Dunn, B. Pseudocapacitive Oxide Materials for High-Rate Electrochemical Energy Storage. *Energy Environ. Sci.* **2014**, *7*, 1597–1614. [[CrossRef](#)]
16. Yan, J.; Liu, T.; Liu, X.; Yan, Y.; Huang, Y. Metal-Organic Framework-Based Materials for Flexible Supercapacitor Application. *Co-ord. Chem. Rev.* **2022**, *452*, 214300. [[CrossRef](#)]
17. Niu, L.; Wu, T.; Chen, M.; Yang, L.; Yang, J.; Wang, Z.; Kornyshev, A.A.; Jiang, H.; Bi, S.; Feng, G. Conductive Metal–Organic Frameworks for Supercapacitors. *Adv. Mater.* **2022**, *34*, e2200999. [[CrossRef](#)]

18. Li, P.; Wang, B. Recent Development and Application of Conductive MOFs. *Isr. J. Chem.* **2018**, *58*, 1010–1018. [[CrossRef](#)]
19. Furukawa, H.; Cordova, K.E.; O’Keeffe, M.; Yaghi, O.M. The Chemistry and Applications of Metal-Organic Frameworks. *Science* **2013**, *341*, 1230444. [[CrossRef](#)]
20. Usman, M.; Haider, G.; Mendiratta, S.; Luo, T.-T.; Chen, Y.-F.; Lu, K.-L. Continuous Broadband Emission from a Metal–Organic Framework as a Human-Friendly White Light Source. *J. Mater. Chem. C* **2016**, *4*, 4728–4732. [[CrossRef](#)]
21. Duan, T.-W.; Yan, B. Hybrids Based on Lanthanide Ions Activated Yttrium Metal–Organic Frameworks: Functional Assembly, Polymer Film Preparation and Luminescence Tuning. *J. Mater. Chem. C* **2014**, *2*, 5098–5104. [[CrossRef](#)]
22. Li, J.-R.; Sculley, J.; Zhou, H.-C. Metal–Organic Frameworks for Separations. *Chem. Rev.* **2011**, *112*, 869–932. [[CrossRef](#)] [[PubMed](#)]
23. Li, B.; Hu, N.; Su, Y.; Yang, Z.; Shao, F.; Li, G.; Zhang, C.; Zhang, Y. Direct Inkjet Printing of Aqueous Inks to Flexible All-Solid-State Graphene Hybrid Micro-Supercapacitors. *ACS Appl. Mater. Interfaces* **2019**, *11*, 46044–46053. [[CrossRef](#)] [[PubMed](#)]
24. Wang, K.B.; Xun, Q.; Zhang, Q. Recent Progress in Metal-Organic Frameworks as Active Materials for Supercapacitors. *Energy Chem.* **2020**, *2*, 100025. [[CrossRef](#)]
25. Hong, M.; Zhou, C.; Xu, S.; Ye, X.; Yang, Z.; Zhang, L.; Zhou, Z.; Hu, N.; Zhang, Y. Bi-Metal Organic Framework Nanosheets Assembled on Nickel Wire Films for Volumetric-Energy-Dense Supercapacitors. *J. Power Sources* **2019**, *423*, 80–89. [[CrossRef](#)]
26. Chaudhari, S.; Sharma, Y.; Archana, P.S.; Jose, R.; Ramakrishna, S.; Mhaisalkar, S.; Srinivasan, M. Electrospun Polyaniline Nanofibers Web Electrodes for Supercapacitors. *J. Appl. Polym. Sci.* **2012**, *129*, 1660–1668. [[CrossRef](#)]
27. Getman, R.B.; Bae, Y.-S.; Wilmer, C.E.; Snurr, R.Q. Review and Analysis of Molecular Simulations of Methane, Hydrogen, and Acetylene Storage in Metal–Organic Frameworks. *Chem. Rev.* **2012**, *112*, 703–723. [[CrossRef](#)] [[PubMed](#)]
28. Rowsell, J.L.C.; Yaghi, O.M. Microporous Materials Strategies for Hydrogen Storage in Metal-Organic Frameworks. *Angew. Chem. Int. Ed.* **2005**, *44*, 4670–4679. [[CrossRef](#)] [[PubMed](#)]
29. Ajdari, F.B.; Kowsari, E.; Shahrak, M.N.; Ehsani, A.; Kiaei, Z.; Torkzaban, H.; Ershadi, M.; Eshkalak, S.K.; Haddadi-Asl, V.; Chinnappan, A.; et al. A review on the Field Patents and Recent Developments Over the Application of Metal Organic Frameworks (MOFs) in Supercapacitors. *Coord. Chem. Rev.* **2020**, *422*, 213441. [[CrossRef](#)]
30. Naseri, M.; Fotouhi, L.; Ehsani, A.; Dehghanpour, S. Facile Electrosynthesis of Nano Flower Like Metal-Organic Framework and its Nanocomposite with Conjugated Polymer as a Novel and Hybrid Electrode Material for Highly Capacitive Pseudocapacitors. *J. Colloid Interface Sci.* **2016**, *484*, 314–319. [[CrossRef](#)]
31. Rahmanifar, M.S.; Hesari, H.; Noori, A.; Masoomi, M.Y.; Morsali, A.; Mousavi, M.F. A Dual Ni/Co-MOF-Reduced Graphene Oxide Nanocomposite as a High Performance Supercapacitor Electrode Material. *Electrochim. Acta* **2018**, *275*, 76–86. [[CrossRef](#)]
32. Shen, D.; Pang, A.; Li, Y.; Dou, J.; Wei, M. Metal–Organic Frameworks at Interfaces of Hybrid Perovskite Solar Cells for Enhanced Photovoltaic Properties. *Chem. Commun.* **2018**, *54*, 1253–1256. [[CrossRef](#)] [[PubMed](#)]
33. He, H.; Hashemi, L.; Hu, M.-L.; Morsali, A. The role of the Counter-Ion in Metal-Organic Frameworks’ Chemistry and Applications. *Coord. Chem. Rev.* **2018**, *376*, 319–347. [[CrossRef](#)]
34. Li, H.; Zhang, Z.; Huang, X.; Lan, T.; Wei, M.; Ma, T. Metal–Organic Framework Derived Hierarchical Porous TiO<sub>2</sub> Nanopills as a Super Stable Anode for Na-ion batteries. *J. Energy Chem.* **2017**, *26*, 667–672. [[CrossRef](#)]
35. Ding, T.; Wu, J.; Chen, Z.; Lan, T.; Wei, M. Synthesis of Hierarchically Mesoporous TiO<sub>2</sub> Spheres via an Emulsion Polymerization Route for Superior Lithium-Ion Batteries. *J. Electroanal. Chem.* **2018**, *818*, 1–9. [[CrossRef](#)]
36. Ryu, H.S.; Park, J.W.; Park, J.; Ahn, J.-P.; Kim, K.-W.; Ahn, J.-H.; Nam, T.-H.; Wang, G.; Ahn, H.-J. High Capacity Cathode Materials for Li-S Batteries. *J. Mater. Chem. A* **2013**, *1*, 1573–1578. [[CrossRef](#)]
37. Ke, F.-S.; Wu, Y.-S.; Deng, H. Metal-Organic Frameworks for Lithium Ion Batteries and Supercapacitors. *J. Solid State Chem.* **2015**, *223*, 109–121. [[CrossRef](#)]
38. Zheng, S.; Li, Q.; Xue, H.; Pang, H.; Xu, Q. A highly Alkaline-Stable Metal Oxide@Metal–Organic Framework Composite for High-Performance Electrochemical Energy Storage. *Natl. Sci. Rev.* **2019**, *7*, 305–314. [[CrossRef](#)]
39. Li, X.; Yang, X.; Xue, H.; Pang, H.; Xu, Q. Metal–Organic Frameworks as a Platform for Clean Energy Applications. *EnergyChem* **2020**, *2*, 100027. [[CrossRef](#)]
40. Liang, Z.; Zhao, R.; Qiu, T.; Zou, R.; Xu, Q. Metal-Organic Framework-Derived Materials for Electrochemical Energy Applications. *EnergyChem* **2019**, *1*, 100001. [[CrossRef](#)]
41. Li, C.; Zhang, L.; Chen, J.; Li, X.; Sun, J.; Zhu, J.; Wang, X.; Fu, Y. Recent Development and Applications of Electrical Conductive MOFs. *Nanoscale* **2021**, *13*, 485–509. [[CrossRef](#)] [[PubMed](#)]
42. Xie, L.S.; Skorupskii, G.; Dincă, M. Electrically Conductive Metal–Organic Frameworks. *Chem. Rev.* **2020**, *120*, 8536–8580. [[CrossRef](#)] [[PubMed](#)]
43. Ding, M.; Cai, X.; Jiang, H.-L. Improving MOF Stability: Approaches and Applications. *Chem. Sci.* **2019**, *10*, 10209–10230. [[CrossRef](#)]
44. Shang, S.; Du, C.; Liu, Y.; Liu, M.; Wang, X.; Gao, W.; Zou, Y.; Dong, J.; Liu, Y.; Chen, J. Publisher Correction: A One-Dimensional Conductive Metal-Organic Framework with Extended  $\pi$ -d Conjugated Nanoribbon Layers. *Nat. Commun.* **2023**, *14*, 190. [[CrossRef](#)] [[PubMed](#)]
45. Hmadeh, M.; Liu, Z.; Gándara, F.; Furukawa, H.; Wan, S.; Augustyn, V.; Chang, R.; Liao, L.; Zhou, F.; Perre, E.; et al. New Porous Crystals of Extended Metal-Catecholates. *Chem. Mater.* **2012**, *24*, 3511–3513. [[CrossRef](#)]
46. Nam, K.W.; Park, S.S.; dos Reis, R.; Dravid, V.P.; Kim, H.; Mirkin, C.A.; Stoddart, J.F. Conductive 2D metal-Organic Framework for High-Performance Cathodes in Aqueous Rechargeable Zinc Batteries. *Nat. Commun.* **2019**, *10*, 4948. [[CrossRef](#)]

47. Gu, S.; Bai, Z.; Majumder, S.; Huang, B.; Chen, G. Conductive Metal–Organic Framework with Redox Metal Center as Cathode for High Rate Performance Lithium Ion Battery. *J. Power Sources* **2019**, *429*, 22–29. [[CrossRef](#)]
48. Li, W.-H.; Ding, K.; Tian, H.-R.; Yao, M.-S.; Nath, B.; Deng, W.-H.; Wang, Y.; Xu, G. Conductive Metal–Organic Framework Nanowire Array Electrodes for High-Performance Solid-State Supercapacitors. *Adv. Funct. Mater.* **2017**, *27*, 1702067. [[CrossRef](#)]
49. Park, C.; Baek, J.W.; Shin, E.; Kim, I.-D. Two-Dimensional Electrically Conductive Metal–Organic Frameworks as Chemiresistive Sensors. *ACS Nanosci. Au* **2023**, *3*, 353–374. [[CrossRef](#)]
50. Chen, H.; Xiao, Y.; Chen, C.; Yang, J.; Gao, C.; Chen, Y.; Wu, J.; Shen, Y.; Zhang, W.; Li, S.; et al. Conductive MOF-Modified Separator for Mitigating the Shuttle Effect of Lithium–Sulfur Battery through a Filtration Method. *ACS Appl. Mater. Interfaces* **2019**, *11*, 11459–11465. [[CrossRef](#)]
51. Cai, D.; Lu, M.; Li, L.; Cao, J.; Chen, D.; Tu, H.; Li, J.; Han, W. A Highly Conductive MOF of Graphene Analogue Ni<sub>3</sub>(HITP)<sub>2</sub> as a Sulfur Host for High-Performance Lithium–Sulfur Batteries. *Small* **2019**, *15*, e1902605. [[CrossRef](#)] [[PubMed](#)]
52. Park, J.; Lee, M.; Feng, D.; Huang, Z.; Hinckley, A.C.; Yakovenko, A.; Zou, X.; Cui, Y.; Bao, Z. Stabilization of Hexaaminobenzene in a 2D Conductive Metal–Organic Framework for High Power Sodium Storage. *J. Am. Chem. Soc.* **2018**, *140*, 10315–10323. [[CrossRef](#)] [[PubMed](#)]
53. Dong, S.; Wu, L.; Xue, M.; Li, Z.; Xiao, D.; Xu, C.; Shen, L.; Zhang, X. Conductive Metal–Organic Framework for High Energy Sodium-Ion Hybrid Capacitors. *ACS Appl. Energy Mater.* **2021**, *4*, 1568–1574. [[CrossRef](#)]
54. Sheberla, D.; Sun, L.; Blood-Forsythe, M.A.; Er, S.; Wade, C.R.; Brozek, C.K.; Aspuru-Guzik, A.; Dincă, M. High Electrical Conductivity in Ni<sub>3</sub>(2,3,6,7,10,11-Hexaiminotriphenylene)<sub>2</sub>, a Semiconducting Metal–Organic Graphene Analogue. *J. Am. Chem. Soc.* **2014**, *136*, 8859–8862. [[CrossRef](#)]
55. Wu, H.; Zhang, W.; Kandambeth, S.; Shekhah, O.; Eddaoudi, M.; Alshareef, H.N. Conductive Metal–Organic Frameworks Selectively Grown on Laser-Scribed Graphene for Electrochemical Microsupercapacitors. *Adv. Energy Mater.* **2019**, *9*, 1900482. [[CrossRef](#)]
56. Wu, Z.; Adekoya, D.; Huang, X.; Kiefel, M.J.; Xie, J.; Xu, W.; Zhang, Q.; Zhu, D.; Zhang, S. Highly Conductive Two-Dimensional Metal–Organic Frameworks for Resilient Lithium Storage with Superb Rate Capability. *ACS Nano* **2020**, *14*, 12016–12026. [[CrossRef](#)] [[PubMed](#)]
57. Wang, S.; Huang, F.; Zhang, Z.; Cai, W.; Jie, Y.; Wang, S.; Yan, P.; Jiao, S.; Cao, R. Conductive Metal–Organic Frameworks Promoting Polysulfides Transformation in Lithium–Sulfur Batteries. *J. Energy Chem.* **2021**, *63*, 336–343. [[CrossRef](#)]
58. Guo, J.; Wu, L.; Ye, Y.-X.; Zhu, F.; Xu, J.; Ouyang, G. Two-Dimensional Conductive Metal–Organic Framework for Small-Molecule Sensing in Aqueous Solution. *Anal. Chem.* **2023**, *95*, 13412–13416. [[CrossRef](#)]
59. Wang, H.; Zhu, C.; Wu, M.; Zheng, F.; Gao, Y.; Niu, H. Synthesis of a Novel Double-Ligand Nickel Conductive Metal–Organic Framework Material and its Electrochemical Characterization for Supercapacitors. *J. Mater. Sci.* **2020**, *56*, 2517–2527. [[CrossRef](#)]
60. Jeon, M.; Kim, M.; Lee, J.-S.; Kim, H.; Choi, S.-J.; Moon, H.R.; Kim, J. Computational Prediction of Stacking Mode in Conductive Two-Dimensional Metal–Organic Frameworks: An Exploration of Chemical and Electrical Property Changes. *ACS Sensors* **2023**, *8*, 3068–3075. [[CrossRef](#)]
61. Van Vleet, M.J.; Weng, T.; Li, X.; Schmidt, J.R. In Situ, Time-Resolved, and Mechanistic Studies of Metal–Organic Framework Nucleation and Growth. *Chem. Rev.* **2018**, *118*, 3681–3721. [[CrossRef](#)]
62. Takaishi, S.; Hosoda, M.; Kajiwara, T.; Miyasaka, H.; Yamashita, M.; Nakanishi, Y.; Kitagawa, Y.; Yamaguchi, K.; Kobayashi, A.; Kitagawa, H. Electroconductive Porous Coordination Polymer Cu[Cu(pdt)<sub>2</sub>] Composed of Donor and Acceptor Building Units. *Inorg. Chem.* **2009**, *48*, 9048–9050. [[CrossRef](#)] [[PubMed](#)]
63. Iqbal, M.Z.; Shaheen, M.; Khan, M.W.; Siddique, S.; Farid, S.; Aftab, S.; Wabaidur, S.M. Elucidating d- $\pi$  Conjugated Two-Dimensional 2,3,6,7,10,11-Hexahydroxytriphenylene based Conductive Metal–Organic Framework for Hybrid Supercapacitors. *J. Electroanal. Chem.* **2023**, *943*, 117564. [[CrossRef](#)]
64. Sirijaraensre, J. Sensing properties of 2D conductive M<sub>3</sub>(HITP)<sub>2</sub> MOFs toward SO<sub>2</sub> gas: A Theoretical Study. *Chem. Pap.* **2023**, *77*, 6053–6068. [[CrossRef](#)]
65. Wrogemann, J.M.; Lüther, M.J.; Bärmann, P.; Lounasvuori, M.; Javed, A.; Tiemann, M.; Golnak, R.; Xiao, J.; Petit, T.; Placke, T.; et al. Overcoming Diffusion Limitation of Faradaic Processes: Property-Performance Relationships of 2D Conductive Metal–Organic Framework Cu<sub>3</sub>(HHTP)<sub>2</sub> for Reversible Lithium-Ion Storage. *Angew. Chem. Int. Ed.* **2023**, *62*, e202303111. [[CrossRef](#)] [[PubMed](#)]
66. Iqbal, M.Z.; Shaheen, M.; Khan, M.W.; Siddique, S.; Farid, S.; Aftab, S.; Wabaidur, S.M. The rise of 2D Conductive Metal–Organic Framework: Cu<sub>3</sub>(HHTP)<sub>2</sub> d- $\pi$  MOF for Integrated Battery–Supercapacitor Hybrids. *Mater. Today Sustain.* **2023**, *22*, 100331. [[CrossRef](#)]
67. Zhao, W.; Chen, T.; Wang, W.; Jin, B.; Peng, J.; Bi, S.; Jiang, M.; Liu, S.; Zhao, Q.; Huang, W. Conductive Ni<sub>3</sub>(HITP)<sub>2</sub> MOFs thin Films for Flexible Transparent Supercapacitors with High Rate Capability. *Sci. Bull.* **2020**, *65*, 1803–1811. [[CrossRef](#)] [[PubMed](#)]
68. Zang, Y.; Pei, F.; Huang, J.; Fu, Z.; Xu, G.; Fang, X. Large-Area Preparation of Crack-Free Crystalline Microporous Conductive Membrane to Upgrade High Energy Lithium–Sulfur Batteries. *Adv. Energy Mater.* **2018**, *8*, 1802052. [[CrossRef](#)]
69. Yan, J.; Cui, Y.; Xie, M.; Yang, G.; Bin, D.; Li, D. Immobilizing Redox-Active Tricycloquinazoline into a 2D Conductive Metal–Organic Framework for Lithium Storage. *Angew. Chem.* **2021**, *133*, 24672–24677. [[CrossRef](#)]
70. Gittins, J.W.; Ballhatchet, C.J.; Chen, Y.; Liu, C.; Madden, D.G.; Britto, S.; Golomb, M.J.; Walsh, A.; Fairen-Jimenez, D.; Dutton, S.E.; et al. Insights Into the Electric Double-Layer Capacitance of Two-Dimensional Electrically Conductive Metal–Organic Frameworks. *J. Mater. Chem. A* **2021**, *9*, 16006–16015. [[CrossRef](#)]

71. Contreras-Pereda, N.; Rodríguez-San-Miguel, D.; Franco, C.; Sevim, S.; Vale, J.P.; Solano, E.; Fong, W.; Del Giudice, A.; Galantini, L.; Pfaltner, R.; et al. 2D Materials: Synthesis of 2D Porous Crystalline Materials in Simulated Microgravity (*Adv. Mater.* 30/2021). *Adv. Mater.* **2021**, *33*, 2170231. [[CrossRef](#)]
72. Wang, M.; Dong, R.; Feng, X. Two-Dimensional Conjugated Metal–Organic Frameworks (2D *c*-MOFs): Chemistry and Function for MOFtronics. *Chem. Soc. Rev.* **2021**, *50*, 2764–2793. [[CrossRef](#)]
73. Wu, G.; Huang, J.; Zang, Y.; He, J.; Xu, G. Porous Field-Effect Transistors Based on a Semiconductive Metal–Organic Framework. *J. Am. Chem. Soc.* **2017**, *139*, 1360–1363. [[CrossRef](#)] [[PubMed](#)]
74. Zhong, Y.; Zhang, X.; He, Y.; Peng, H.; Wang, G.; Xin, G. Simultaneously Armored and Active Graphene for Transparent and Flexible Supercapacitors. *Adv. Funct. Mater.* **2018**, *28*, 1801998. [[CrossRef](#)]
75. Peng, H.; Zhong, Y.; Zhang, X.; He, Y.; Wang, G. Percolating Film of Pillared Graphene Layer Integrated with Silver Nanowire Network for Transparent and Flexible Supercapacitors. *Langmuir* **2018**, *34*, 15245–15252. [[CrossRef](#)] [[PubMed](#)]
76. Wang, G.-F.; Qin, H.; Gao, X.; Cao, Y.; Wang, W.; Wang, F.-C.; Wu, H.-A.; Cong, H.-P.; Yu, S.-H. Graphene Thin Films by Noncovalent-Interaction-Driven Assembly of Graphene Monolayers for Flexible Supercapacitors. *Chem* **2018**, *4*, 896–910. [[CrossRef](#)]
77. Majidi, L.; Ahmadiparidari, A.; Shan, N.; Singh, S.K.; Zhang, C.; Huang, Z.; Rastegar, S.; Kumar, K.; Hemmat, Z.; Ngo, A.T.; et al. Nanostructured Conductive Metal Organic Frameworks for Sustainable Low Charge Overpotentials in Li–Air Batteries. *Small* **2022**, *18*, 2102902. [[CrossRef](#)] [[PubMed](#)]
78. Kon, K.; Uchida, K.; Fuku, K.; Yamanaka, S.; Wu, B.; Yamazui, D.; Iguchi, H.; Kobayashi, H.; Gambe, Y.; Honma, I.; et al. Electron-Conductive Metal–Organic Framework, Fe(Dhbq)(Dhbq = 2,5-Dihydroxy-1,4-Benzoquinone): Coexistence of Microporosity and Solid-State Redox Activity. *ACS Appl. Mater. Interfaces* **2021**, *13*, 38188–38193. [[CrossRef](#)] [[PubMed](#)]
79. Zhou, S.; Kong, X.; Zheng, B.; Huo, F.; Strømme, M.; Xu, C. Cellulose Nanofiber @ Conductive Metal–Organic Frameworks for High-Performance Flexible Supercapacitors. *ACS Nano* **2019**, *13*, 9578–9586. [[CrossRef](#)] [[PubMed](#)]
80. Kambe, T.; Sakamoto, R.; Hoshiko, K.; Takada, K.; Miyachi, M.; Ryu, J.-H.; Sasaki, S.; Kim, J.; Nakazato, K.; Takata, M.; et al.  $\pi$ -Conjugated Nickel Bis(dithiolene) Complex Nanosheet. *J. Am. Chem. Soc.* **2013**, *135*, 2462–2465. [[CrossRef](#)] [[PubMed](#)]
81. Rubio-Giménez, V.; Galbiati, M.; Castells-Gil, J.; Almora-Barrios, N.; Navarro-Sánchez, J.; Escorcia-Ariza, G.; Mattera, M.; Arnold, T.; Rawle, J.; Tatay, S.; et al. Bottom-Up Fabrication of Semiconductive Metal–Organic Framework Ultrathin Films. *Adv. Mater.* **2018**, *30*, 1704291. [[CrossRef](#)] [[PubMed](#)]
82. Du, X.; Zhang, J.; Wang, H.; Huang, Z.; Guo, A.; Zhao, L.; Niu, Y.; Li, X.; Wu, B.; Liu, Y. Solid–Solid Interface Growth of Conductive Metal–Organic Framework Nanowire Arrays and their Supercapacitor Application. *Mater. Chem. Front.* **2019**, *4*, 243–251. [[CrossRef](#)]
83. Guo, J.; Liu, J.; Ma, W.; Sang, Z.; Yin, L.; Zhang, X.; Chen, H.; Liang, J.; Yang, D. Vanadium Oxide Intercalated with Conductive Metal–Organic Frameworks with Dual Energy-Storage Mechanism for High Capacity and High-Rate Capability Zn Ion Storage. *Adv. Funct. Mater.* **2023**, *33*, 2302659. [[CrossRef](#)]
84. Li, P.; Shi, X.; Wu, Y.; Song, M.; Lai, Y.; Yu, H.; Lu, G. Cathodic synthesis of a Cu-Catecholate Metal–Organic Framework. *CrystEngComm* **2021**, *23*, 1828–1835. [[CrossRef](#)]
85. Choi, J.Y.; Park, J. Enhancing Electrical Conductivity of Semiconducting MOFs via Defect Healing. *ACS Appl. Electron. Mater.* **2021**, *3*, 4197–4202. [[CrossRef](#)]
86. Varoon, K.; Zhang, X.; Elyassi, B.; Brewer, D.D.; Gettel, M.; Kumar, S.; Lee, J.A.; Maheshwari, S.; Mittal, A.; Sung, C.Y.; et al. Dispersible Exfoliated Zeolite Nanosheets and Their Application as a Selective Membrane. *Science* **2011**, *334*, 72–75. [[CrossRef](#)] [[PubMed](#)]
87. Iqbal, R.; Sultan, M.Q.; Hussain, S.; Hamza, M.; Tariq, A.; Akbar, M.B.; Ma, Y.; Zhi, L. The Different Roles of Cobalt and Manganese in Metal–Organic Frameworks for Supercapacitors. *Adv. Mater. Technol.* **2021**, *6*, 2000941. [[CrossRef](#)]
88. Guo, T.; Ding, Y.; Xu, C.; Bai, W.; Pan, S.; Liu, M.; Bi, M.; Sun, J.; Ouyang, X.; Wang, X.; et al. High Crystallinity 2D  $\pi$ -d Conjugated Conductive Metal–Organic Framework for Boosting Polysulfide Conversion in Lithium–Sulfur Batteries. *Adv. Sci.* **2023**, *10*, e2302518. [[CrossRef](#)]
89. Jia, H.; Lu, S.; Shin, S.H.R.; Sushko, M.L.; Tao, X.; Hummel, M.; Thallapally, P.K.; Liu, J.; Gu, Z. In Situ Anodic Electrodeposition of Two-Dimensional Conductive Metal–Organic Framework@Nickel Foam for high-Performance Flexible Supercapacitor. *J. Power Sources* **2022**, *526*, 231163. [[CrossRef](#)]
90. Sang, Z.; Liu, J.; Zhang, X.; Yin, L.; Hou, F.; Liang, J. One-Dimensional  $\pi$ -d Conjugated Conductive Metal–Organic Framework with Dual Redox-Active Sites for High-Capacity and Durable Cathodes for Aqueous Zinc Batteries. *ACS Nano* **2023**, *17*, 3077–3087. [[CrossRef](#)]
91. Chen, X.; Dong, J.; Chi, K.; Wang, L.; Xiao, F.; Wang, S.; Zhao, Y.; Liu, Y. Electrically Conductive Metal–Organic Framework Thin Film-Based On-Chip Micro-Biosensor: A Platform to Unravel Surface Morphology-Dependent Biosensing. *Adv. Funct. Mater.* **2021**, *31*, 2102855. [[CrossRef](#)]
92. Chen, X.; Lu, Y.; Dong, J.; Ma, L.; Yi, Z.; Wang, Y.; Wang, L.; Wang, S.; Zhao, Y.; Huang, J.; et al. Ultrafast *In Situ* Synthesis of Large-Area Conductive Metal–Organic Frameworks on Substrates for Flexible Chemiresistive Sensing. *ACS Appl. Mater. Interfaces* **2020**, *12*, 57235–57244. [[CrossRef](#)] [[PubMed](#)]

93. Feng, D.; Lei, T.; Lukatskaya, M.R.; Park, J.; Huang, Z.; Lee, M.; Shaw, L.; Chen, S.; Yakovenko, A.A.; Kulkarni, A.; et al. Robust and Conductive Two-Dimensional Metal–Organic Frameworks with Exceptionally High Volumetric and areal Capacitance. *Nat. Energy* **2018**, *3*, 30–36. [[CrossRef](#)]
94. Park, J.; Hinckley, A.C.; Huang, Z.; Chen, G.; Yakovenko, A.A.; Zou, X.; Bao, Z. High Thermopower in a Zn-Based 3D Semi-conductive Metal–Organic Framework. *J. Am. Chem. Soc.* **2020**, *142*, 20531–20535. [[CrossRef](#)] [[PubMed](#)]
95. Sun, L.; Liao, B.; Sheberla, D.; Kraemer, D.; Zhou, J.; Stach, E.A.; Zakharov, D.; Stavila, V.; Talin, A.A.; Ge, Y.; et al. A Microporous and Naturally Nanostructured Thermoelectric Metal–Organic Framework with Ultralow Thermal Conductivity. *Joule* **2017**, *1*, 168–177. [[CrossRef](#)]
96. Yao, M.-S.; Lv, X.-J.; Fu, Z.-H.; Li, W.-H.; Deng, W.-H.; Wu, G.-D.; Xu, G. Inside Cover: Layer-by-Layer Assembled Conductive Metal–Organic Framework Nanofilms for Room-Temperature Chemiresistive Sensing (Angew. Chem. Int. Ed. 52/2017). *Angew. Chem. Int. Ed.* **2017**, *56*, 16418. [[CrossRef](#)]
97. Lai, X.; Peng, J.; Cheng, Q.; Tomsia, A.P.; Zhao, G.; Liu, L.; Zou, G.; Song, Y.; Jiang, L.; Li, M. Cover Picture: Bioinspired Color Switchable Photonic Crystal Silicone Elastomer Kirigami (Angew. Chem. Int. Ed. 26/2021). *Angew. Chem. Int. Ed.* **2021**, *60*, 14197. [[CrossRef](#)]
98. Meng, Z.; Aykanat, A.; Mirica, K.A. Welding Metallophthalocyanines into Bimetallic Molecular Meshes for Ultrasensitive, Low-Power Chemiresistive Detection of Gases. *J. Am. Chem. Soc.* **2018**, *141*, 2046–2053. [[CrossRef](#)]
99. Howarth, A.J.; Peters, A.W.; Vermeulen, N.A.; Wang, T.C.; Hupp, J.T.; Farha, O.K. Best Practices for the Synthesis, Activation, and Characterization of Metal–Organic Frameworks. *Chem. Mater.* **2017**, *29*, 26–39. [[CrossRef](#)]
100. Saeki, A.; Koizumi, Y.; Aida, T.; Seki, S. Comprehensive Approach to Intrinsic Charge Carrier Mobility in Conjugated Organic Molecules, Macromolecules, and Supramolecular Architectures. *Accounts Chem. Res.* **2012**, *45*, 1193–1202. [[CrossRef](#)] [[PubMed](#)]
101. Givaja, G.; Amo-Ochoa, P.; Gomez-Garcia, C.J.; Zamora, F. Electrical conductive coordination polymers. *Chem. Soc. Rev.* **2012**, *41*, 115–147. [[CrossRef](#)]
102. Wilmer, C.E.; Leaf, M.; Lee, C.Y.; Farha, O.K.; Hauser, B.G.; Hupp, J.T.; Snurr, R.Q. Large-Scale Screening of Hypothetical Metal–organic frameworks. *Nat. Chem.* **2012**, *4*, 83–89. [[CrossRef](#)] [[PubMed](#)]
103. Yan, Y.; Lin, X.; Ge, J.; Li, X. Conductive Metal–Organic Frameworks with Wheel-Shaped Metallomacrocyclic Subunits as High-Performance Supercapacitor Electrodes. *Chem. Eng. J.* **2023**, *468*, 143739. [[CrossRef](#)]
104. Liu, P.; Yan, J.; Huang, H.; Song, W. Cu/Co bimetallic conductive MOFs: Electronic Modulation for Enhanced Nitrate Reduction to Ammonia. *Chem. Eng. J.* **2023**, *466*, 143134. [[CrossRef](#)]
105. Wang, T.C.; Bury, W.; Gómez-Gualdrón, D.A.; Vermeulen, N.A.; Mondloch, J.E.; Deria, P.; Zhang, K.; Moghadam, P.Z.; Sarjeant, A.A.; Snurr, R.Q.; et al. Ultrahigh Surface Area Zirconium MOFs and Insights into the Applicability of the BET Theory. *J. Am. Chem. Soc.* **2015**, *137*, 3585–3591. [[CrossRef](#)] [[PubMed](#)]
106. Gómez-Gualdrón, D.A.; Moghadam, P.Z.; Hupp, J.T.; Farha, O.K.; Snurr, R.Q. Application of Consistency Criteria to Calculate BET Areas of Micro- and Mesoporous Metal–Organic Frameworks. *J. Am. Chem. Soc.* **2016**, *138*, 215–224. [[CrossRef](#)]
107. Sun, X.; Yan, X.; Song, K.; Zhang, T.; Yang, Z.; Su, X.; Chen, W.; Chen, L. A Pyrazine-Based 2D Conductive Metal–Organic Framework for Efficient Lithium Storage<sup>†</sup>. *Chin. J. Chem.* **2023**, *41*, 1691–1696. [[CrossRef](#)]
108. Liu, J.; Zhou, Y.; Xie, Z.; Li, Y.; Liu, Y.; Sun, J.; Ma, Y.; Terasaki, O.; Chen, L. Conjugated Copper–Catecholate Framework Electrodes for Efficient Energy Storage. *Angew. Chem. Int. Ed.* **2019**, *59*, 1081–1086. [[CrossRef](#)]
109. Wu, T.; Ma, Z.; He, Y.; Wu, X.; Tang, B.; Yu, Z.; Wu, G.; Chen, S.; Bao, N. A Covalent Black Phosphorus/Metal–Organic Framework Hetero-nanostructure for High-Performance Flexible Supercapacitors. *Angew. Chem. Int. Ed.* **2021**, *60*, 10366–10374. [[CrossRef](#)] [[PubMed](#)]
110. Xia, Z.; Jia, X.; Ge, X.; Ren, C.; Yang, Q.; Hu, J.; Chen, Z.; Han, J.; Xie, G.; Chen, S.; et al. Tailoring Electronic Structure and Size of Ultrastable Metalated Metal–Organic Frameworks with Enhanced Electroconductivity for High-Performance Supercapacitors. *Angew. Chem.* **2021**, *133*, 10316–10326. [[CrossRef](#)]
111. Choi, J.Y.; Wang, M.; Check, B.; Stodolka, M.; Tayman, K.; Sharma, S.; Park, J. Linker-Based Bandgap Tuning in Conductive MOF Solid Solutions. *Small* **2023**, *19*, e2206988. [[CrossRef](#)] [[PubMed](#)]
112. Vukotic, V.N.; Harris, K.J.; Zhu, K.; Schurko, R.W.; Loeb, S.J. Metal–Organic Frameworks with Dynamic Interlocked Components. *Nat. Chem.* **2012**, *4*, 456–460. [[CrossRef](#)] [[PubMed](#)]
113. Zhu, K.; O’Keefe, C.A.; Vukotic, V.N.; Schurko, R.W.; Loeb, S.J. A molecular Shuttle that Operates Inside a Metal–Organic Framework. *Nat. Chem.* **2015**, *7*, 514–519. [[CrossRef](#)] [[PubMed](#)]
114. Brozek, C.K.; Michaelis, V.K.; Ong, T.-C.; Bellarosa, L.; López, N.; Griffin, R.G.; Dincă, M. Dynamic DMF Binding in MOF-5 Enables the Formation of Metastable Cobalt-Substituted MOF-5 Analogues. *ACS Cent. Sci.* **2015**, *1*, 252–260. [[CrossRef](#)] [[PubMed](#)]
115. Rimoldi, M.; Nakamura, A.; Vermeulen, N.A.; Henkelis, J.J.; Blackburn, A.K.; Hupp, J.T.; Stoddart, J.F.; Farha, O.K. A metal–organic framework immobilised iridium pincer complex. *Chem. Sci.* **2016**, *7*, 4980–4984. [[CrossRef](#)] [[PubMed](#)]
116. Mason, J.A.; Sumida, K.; Herm, Z.R.; Krishna, R.; Long, J.R. Evaluating Metal–Organic Frameworks for Post-Combustion Carbon Dioxide Capture via Temperature Swing Adsorption. *Energy Environ. Sci.* **2011**, *4*, 3030–3040. [[CrossRef](#)]
117. Wharmby, M.T.; Henke, S.; Bennett, T.D.; Bajpe, S.R.; Schwedler, I.; Thompson, S.P.; Gozzo, F.; Simoncic, P.; Mellot-Draznieks, C.; Tao, H.; et al. Extreme Flexibility in a Zeolitic Imidazolate Framework: Porous to Dense Phase Transition in Desolvated ZIF-4. *Angew. Chem.* **2015**, *127*, 6547–6551. [[CrossRef](#)]



118. Liu, D.; Huxford, R.C.; Lin, W. Phosphorescent Nanoscale Coordination Polymers as Contrast Agents for Optical Imaging. *Angew. Chem. Int. Ed.* **2011**, *50*, 3696–3700. [[CrossRef](#)]
119. Fei, H.; Shin, J.; Meng, Y.S.; Adelhardt, M.; Sutter, J.; Meyer, K.; Cohen, S.M. Reusable Oxidation Catalysis Using Met-al-Monocatecholato Species in a Robust Metal-Organic Framework. *J. Am. Chem. Soc.* **2014**, *136*, 4965–4973. [[CrossRef](#)]
120. Wada, K.; Sakaushi, K.; Sasaki, S.; Nishihara, H. Multielectron-Transfer-based Rechargeable Energy Storage of Two-Dimensional Coordination Frameworks with Non-Innocent Ligands. *Angew. Chem.* **2018**, *130*, 9024–9028. [[CrossRef](#)]
121. Gao, G.; Zheng, F.; Pan, F.; Wang, L. Theoretical Investigation of 2D Conductive Microporous Coordination Polymers as Li-S Battery Cathode with Ultrahigh Energy Density. *Adv. Energy Mater.* **2018**, *8*, 1801823. [[CrossRef](#)]
122. Zhang, M.-C.; Liu, M.-Y.; Yang, M.-X.; Liu, X.-X.; Shen, S.-Y.; Wu, J.-S.; Pei, W.-B. Copper-Cobalt Bimetallic Conductive Metal-Organic Frameworks as Bifunctional Oxygen Electrocatalyst in Alkaline and Neutral Media. *J. Solid State Chem.* **2023**, *325*, 124133. [[CrossRef](#)]
123. Miner, E.M.; Fukushima, T.; Sheberla, D.; Sun, L.; Surendranath, Y.; Dincă, M. Electrochemical Oxygen Reduction Catalysed by Ni<sub>3</sub>(hexaiminotriphenylene)<sub>2</sub>. *Nat. Commun.* **2016**, *7*, 10942. [[CrossRef](#)] [[PubMed](#)]
124. Sun, L.; Park, S.S.; Sheberla, D.; Dincă, M. Measuring and Reporting Electrical Conductivity in Metal-Organic Frameworks: Cd<sub>2</sub>(TTFTB) as a Case Study. *J. Am. Chem. Soc.* **2016**, *138*, 14772–14782. [[CrossRef](#)] [[PubMed](#)]
125. Yin, J.; Li, N.; Liu, M.; Li, Z.; Wang, X.; Cheng, M.; Zhong, M.; Li, W.; Xu, Y.; Bu, X. Stabilizing Redox-Active Hexaazatriphenylene in a 2D Conductive Metal-Organic Framework for Improved Lithium Storage Performance. *Adv. Funct. Mater.* **2023**, *33*, 2211950. [[CrossRef](#)]
126. Ohata, T.; Nomoto, A.; Watanabe, T.; Hirosawa, I.; Makita, T.; Takeya, J.; Makiura, R. Air/Liquid Interfacial Formation Process of Conductive Metal-Organic Framework Nanosheets. *J. Colloid Interface Sci.* **2023**, *651*, 769–784. [[CrossRef](#)]
127. Sun, L.; Campbell, M.G.; Dincă, M. Electrically Conductive Porous Metal-Organic Frameworks. *Angew. Chem. Int. Ed.* **2016**, *55*, 3566–3579. [[CrossRef](#)]
128. Dong, J.; Chen, X.; Wang, L.; Wang, S.; Zhao, Y.; Liu, Y. Electrocatalytic Microdevice Array Based on Wafer-Scale Conductive Metal-Organic Framework Thin Film for Massive Hydrogen Production. *Small* **2023**, e2302913. [[CrossRef](#)]
129. Debela, T.T.; Yang, M.C.; Hendon, C.H. Ligand-Mediated Hydrogenic Defects in Two-Dimensional Electrically Conductive Metal-Organic Frameworks. *J. Am. Chem. Soc.* **2023**, *145*, 11387–11391. [[CrossRef](#)]
130. Wang, T.; Lei, J.; Wang, Y.; Pang, L.; Pan, F.; Chen, K.; Wang, H. Approaches to Enhancing Electrical Conductivity of Pristine Metal-Organic Frameworks for Supercapacitor Applications. *Small* **2022**, *18*, e2203307. [[CrossRef](#)] [[PubMed](#)]
131. Nguyen, D.; Schepisi, I.; Amir, F. Extraordinary cycling stability of Ni<sub>3</sub>(HITP)<sub>2</sub> supercapacitors fabricated by electrophoretic deposition: Cycling at 100,000 cycles. *Chem. Eng. J.* **2019**, *378*, 122150. [[CrossRef](#)]
132. He, B.; Zhang, Q.; Man, P.; Zhou, Z.; Li, C.; Li, Q.; Xie, L.; Wang, X.; Pang, H.; Yao, Y. Self-Sacrificed Synthesis of Conductive Vanadium-Based Metal-Organic Framework Nanowire-Bundle Arrays as Binder-Free Cathodes for High-Rate and High-Energy-Density Wearable Zn-Ion Batteries. *Nano Energy* **2019**, *64*, 103935. [[CrossRef](#)]
133. Li, C.; Zhang, Q.; Li, T.; He, B.; Man, P.; Zhu, Z.; Zhou, Z.; Wei, L.; Zhang, K.; Hong, G.; et al. Nickel Metal-Organic Framework Nanosheets as Novel Binder-Free Cathode for Advanced Fibrous Aqueous Rechargeable Ni-Zn battery. *J. Mater. Chem. A* **2020**, *8*, 3262–3269. [[CrossRef](#)]
134. Dresselhaus, M.S.; Thomas, I.L. Alternative energy technologies. *Nature* **2001**, *414*, 332–337. [[CrossRef](#)] [[PubMed](#)]
135. Li, G.; Yang, H.; Li, F.; Cheng, F.; Shi, W.; Chen, J.; Cheng, P. A Coordination Chemistry Approach for Lithium-Ion Batteries: The Coexistence of Metal and Ligand Redox Activities in a One-Dimensional Metal-Organic Material. *Inorg. Chem.* **2016**, *55*, 4935–4940. [[CrossRef](#)] [[PubMed](#)]
136. Holland, B.T.; Blanford, C.F.; Stein, A.; Zakhidov, A.; Baughman, R.H.; Iqbal, Z.; Cui, C.; Khayrullin, I.; Liu, L.; Udod, I.; et al. Three Dimensionally Periodic Structural Assemblies on Nanometer and Longer Scales. US Patent 6,261,469, 10 September 1998.
137. Guo, L.; Sun, J.; Zhang, W.; Hou, L.; Liang, L.; Liu, Y.; Yuan, C. Bottom-Up Fabrication of 1D Cu-based Conductive Metal-Organic Framework Nanowires as a High-Rate Anode towards Efficient Lithium Storage. *ChemSusChem* **2019**, *12*, 5051–5058. [[CrossRef](#)] [[PubMed](#)]
138. Wu, Q.; Yao, Z.; Zhou, X.; Xu, J.; Cao, F.; Li, C. Built-In Catalysis in Confined Nanoreactors for High-Loading Li-S Batteries. *ACS Nano* **2020**, *14*, 3365–3377. [[CrossRef](#)] [[PubMed](#)]
139. Ansari, Y.; Zhang, S.; Wen, B.; Fan, F.; Chiang, Y. Stabilizing Li-S Battery Through Multilayer Encapsulation of Sulfur. *Adv. Energy Mater.* **2019**, *9*, 1802213. [[CrossRef](#)]
140. Hong, S.Y.; Kim, Y.; Park, Y.; Choi, A.; Choi, N.-S.; Lee, K.T. Charge Carriers in Rechargeable Batteries: Na Ions vs. Li Ions. *Energy Environ. Sci.* **2013**, *6*, 2067–2081. [[CrossRef](#)]
141. Palomares, V.; Casas-Cabanas, M.; Castillo-Martínez, E.; Han, M.H.; Rojo, T. Update on Na-Based Battery Materials. A Growing Research Path. *Energy Environ. Sci.* **2013**, *6*, 2312–2337. [[CrossRef](#)]
142. Li, C.; Sun, X.; Yao, Y.; Hong, G. Recent Advances of Electrically Conductive Metal-Organic Frameworks in Electrochemical Applications. *Mater. Today Nano* **2021**, *13*, 100105. [[CrossRef](#)]
143. Zhou, W.; Lv, S.; Liu, X.; Li, Y.; Liu, J. A directly grown pristine Cu-CAT Metal-Organic Framework as an Anode Material for High-Energy Sodium-Ion Capacitors. *Chem. Commun.* **2019**, *55*, 11207–11210. [[CrossRef](#)] [[PubMed](#)]

144. Wang, F.; Liu, Z.; Yang, C.; Zhong, H.; Nam, G.; Zhang, P.; Dong, R.; Wu, Y.; Cho, J.; Zhang, J.; et al. Fully Conjugated Phthalocyanine Copper Metal–Organic Frameworks for Sodium–Iodine Batteries with Long-Time-Cycling Durability. *Adv. Mater.* **2020**, *32*, 1905361. [[CrossRef](#)] [[PubMed](#)]
145. Zhu, K.; Wu, T.; Sun, S.; Wen, Y.; Huang, K. Electrode Materials for Practical Rechargeable Aqueous Zn-Ion Batteries: Challenges and Opportunities. *ChemElectroChem* **2020**, *7*, 2714–2734. [[CrossRef](#)]
146. Song, M.; Tan, H.; Chao, D.; Fan, H.J. Recent Advances in Zn-Ion Batteries. *Adv. Funct. Mater.* **2018**, *28*, 1802564. [[CrossRef](#)]
147. Li, C.; Zheng, C.; Jiang, H.; Bai, S.; Jia, J. Conductive flower-like Ni-PTA-Mn as Cathode for Aqueous Zinc-Ion Batteries. *J. Alloy. Compd.* **2021**, *882*, 160587. [[CrossRef](#)]
148. Chu, S.; Majumdar, A. Opportunities and Challenges for a Sustainable Energy Future. *Nature* **2012**, *488*, 294–303. [[CrossRef](#)]
149. Downes, C.A.; Marinescu, S.C. Electrocatalytic Metal–Organic Frameworks for Energy Applications. *ChemSusChem* **2017**, *10*, 4374–4392. [[CrossRef](#)]
150. Huang, X.; Yao, H.; Cui, Y.; Hao, W.; Zhu, J.; Xu, W.; Zhu, D. Conductive Copper Benzenehexathiol Coordination Polymer as a Hydrogen Evolution Catalyst. *ACS Appl. Mater. Interfaces* **2017**, *9*, 40752–40759. [[CrossRef](#)]
151. Xing, D.; Wang, Y.; Zhou, P.; Liu, Y.; Wang, Z.; Wang, P.; Zheng, Z.; Cheng, H.; Dai, Y.; Huang, B. Co<sub>3</sub>(hexaiminotriphenylene)<sub>2</sub>: A Conductive Two-Dimensional  $\pi$ -d Conjugated Metal–Organic Framework for Highly Efficient Oxygen Evolution Reaction. *Appl. Catal. B Environ.* **2020**, *278*, 119295. [[CrossRef](#)]
152. Duan, J.; Chen, S.; Zhao, C. Ultrathin Metal–Organic Framework Array for Efficient Electrocatalytic Water Splitting. *Nat. Commun.* **2017**, *8*, 15341. [[CrossRef](#)] [[PubMed](#)]
153. Sun, X.; Wu, K.-H.; Sakamoto, R.; Kusamoto, T.; Maeda, H.; Ni, X.; Jiang, W.; Liu, F.; Sasaki, S.; Masunaga, H.; et al. Bis(aminothiolo)nickel Nanosheet as a Redox Switch for Conductivity and an Electrocatalyst for the Hydrogen Evolution Reaction. *Chem. Sci.* **2017**, *8*, 8078–8085. [[CrossRef](#)] [[PubMed](#)]
154. Grimaud, A.; Diaz-Morales, O.; Han, B.; Hong, W.T.; Lee, Y.-L.; Giordano, L.; Stoerzinger, K.A.; Koper, M.T.M.; Shao-Horn, Y. Activating Lattice Oxygen Redox Reactions in Metal Oxides to Catalyse Oxygen Evolution. *Nat. Chem.* **2017**, *9*, 457–465. [[CrossRef](#)] [[PubMed](#)]
155. You, B.; Sun, Y. Innovative Strategies for Electrocatalytic Water Splitting. *Accounts Chem. Res.* **2018**, *51*, 1571–1580. [[CrossRef](#)] [[PubMed](#)]
156. Walter, M.G.; Warren, E.L.; McKone, J.R.; Boettcher, S.W.; Mi, Q.; Santori, E.A.; Lewis, N.S. Solar Water Splitting Cells. *Chem. Rev.* **2010**, *110*, 6446–6473. [[CrossRef](#)] [[PubMed](#)]
157. Hunter, B.M.; Gray, H.B.; Müller, A.M. Earth-Abundant Heterogeneous Water Oxidation Catalysts. *Chem. Rev.* **2016**, *116*, 14120–14136. [[CrossRef](#)]
158. Zhang, C.; Chen, Z.; Lian, Y.; Chen, Y.; Li, Q.; Gu, Y.; Lu, Y.; Deng, Z.; Peng, Y. Copper-based Conductive Metal Organic Framework *In-situ* Grown on Copper Foam as a Bifunctional Electrocatalyst. *Acta Phys.-Chim. Sin.* **2019**, *35*, 1404–1411.
159. Jia, H.; Yao, Y.; Zhao, J.; Gao, Y.; Luo, Z.; Du, P. A Novel Two-Dimensional Nickel Phthalocyanine-Based Metal–Organic Framework for Highly Efficient Water Oxidation Catalysis. *J. Mater. Chem. A* **2018**, *6*, 1188–1195. [[CrossRef](#)]
160. Li, W.-H.; Lv, J.; Li, Q.; Xie, J.; Ogiwara, N.; Huang, Y.; Jiang, H.; Kitagawa, H.; Xu, G.; Wang, Y. Conductive Metal–Organic Framework Nanowire Arrays for Electrocatalytic Oxygen Evolution. *J. Mater. Chem. A* **2019**, *7*, 10431–10438. [[CrossRef](#)]
161. Zhang, J.; Sasaki, K.; Sutter, E.; Adzic, R.R. Stabilization of Platinum Oxygen-Reduction Electrocatalysts Using Gold Clusters. *Science* **2007**, *315*, 220–222. [[CrossRef](#)]
162. Tian, X.; Zhao, X.; Su, Y.-Q.; Wang, L.; Wang, H.; Dang, D.; Chi, B.; Liu, H.; Hensen, E.J.; Lou, X.W.; et al. Engineering Bunched Pt-Ni alloy Nanocages for Efficient Oxygen Reduction in Practical Fuel Cells. *Science* **2019**, *366*, 850–856. [[CrossRef](#)]
163. Kim, J.; Lee, Y.; Sun, S. Structurally Ordered FePt Nanoparticles and Their Enhanced Catalysis for Oxygen Reduction Reaction. *J. Am. Chem. Soc.* **2010**, *132*, 4996–4997. [[CrossRef](#)] [[PubMed](#)]
164. Stamenkovic, V.R.; Fowler, B.; Mun, B.S.; Wang, G.; Ross, P.N.; Lucas, C.A.; Markovic, N.M. Improved Oxygen Reduction Activity on Pt<sub>3</sub>Ni(111) via Increased Surface Site Availability. *Science* **2007**, *315*, 493–497. [[CrossRef](#)]
165. Yoon, H.; Lee, S.; Oh, S.; Park, H.; Choi, S.; Oh, M. Synthesis of Bimetallic Conductive 2D Metal–Organic Framework (Co<sub>x</sub>Ni<sub>y</sub>-CAT) and Its Mass Production: Enhanced Electrochemical Oxygen Reduction Activity. *Small* **2019**, *15*, e1805232. [[CrossRef](#)] [[PubMed](#)]
166. Zhong, H.; Ly, K.H.; Wang, M.; Krupskaya, Y.; Han, X.; Zhang, J.; Zhang, J.; Kataev, V.; Büchner, B.; Weidinger, I.M.; et al. A Phthalocyanine-Based Layered Two-Dimensional Conjugated Metal–Organic Framework as a Highly Efficient Electrocatalyst for the Oxygen Reduction Reaction. *Angew. Chem. Int. Ed.* **2019**, *58*, 10677–10682. [[CrossRef](#)] [[PubMed](#)]
167. Chen, X.; Li, W.; Zhang, G.; Sun, F.; Jing, Q.; Pang, H. Highly Stable and Activated Cerium-Based MOFs Superstructures for Ultrahigh Selective Uranium (VI) Capture from Simulated Seawater. *Mater. Today Chem.* **2021**, *23*, 100705. [[CrossRef](#)]
168. Zhang, G.; Li, Y.; Xiao, X.; Shan, Y.; Bai, Y.; Xue, H.G.; Pang, H.; Tian, Z.; Xu, Q. In Situ Anchoring Polymetallic Phosphide Nanoparticles within Porous Prussian Blue Analogue Nanocages for Boosting Oxygen Evolution Catalysis. *Nano Lett.* **2021**, *21*, 3016–3025. [[CrossRef](#)] [[PubMed](#)]
169. Du, M.; Li, Q.; Zhang, G.; Wang, F.; Pang, H. Metal–Organic Framework-Based Sulfur-Loaded Materials. *Energy Environ. Mater.* **2022**, *5*, 215–230. [[CrossRef](#)]
170. Yin, W.; Zhang, G.; Wang, X.; Pang, H. One–Dimensional Metal–Organic Frameworks for Electrochemical Applications. *Adv. Colloid Interface Sci.* **2021**, *298*, 102562. [[CrossRef](#)] [[PubMed](#)]

171. Wu, J.-X.; Hou, S.-Z.; Zhang, X.-D.; Xu, M.; Yang, H.-F.; Cao, P.-S.; Gu, Z.-Y. Cathodized Copper Porphyrin Metal–Organic Framework Nanosheets for Selective Formate and Acetate Production from CO<sub>2</sub> Electroreduction. *Chem. Sci.* **2019**, *10*, 2199–2205. [[CrossRef](#)]
172. Wang, X.; Zhang, G.; Yin, W.; Zheng, S.; Kong, Q.; Tian, J.; Pang, H. Metal–Organic Framework-Derived Phosphide Nanomaterials for Electrochemical Applications. *Carbon Energy* **2022**, *4*, 246–281. [[CrossRef](#)]
173. Wu, X.; Ru, Y.; Bai, Y.; Zhang, G.; Shi, Y.; Pang, H. PBA Composites and their Derivatives in Energy and Environmental Applications. *Coord. Chem. Rev.* **2022**, *451*, 214260. [[CrossRef](#)]
174. Zhang, G.; Jin, L.; Zhang, R.; Bai, Y.; Zhu, R.; Pang, H. Recent Advances in the Development of Electronically and Ionically Conductive Metal–Organic Frameworks. *Coord. Chem. Rev.* **2021**, *439*, 213915. [[CrossRef](#)]

**Disclaimer/Publisher’s Note:** The statements, opinions and data contained in all publications are solely those of the individual author(s) and contributor(s) and not of MDPI and/or the editor(s). MDPI and/or the editor(s) disclaim responsibility for any injury to people or property resulting from any ideas, methods, instructions or products referred to in the content.